ISTANBUL TECHNICAL UNIVERSITY ★ GRADUATE SCHOOL

LARGE SCALE WIRELESS PROPAGATION CHANNEL CHARACTERIZATION OF AIR-TO-AIR AND AIR-TO-GROUND DRONE COMMUNICATIONS

M.Sc. THESIS

Ubeydullah ERDEMİR

Department of Electronics and Communication Engineering

Telecommunication Engineering Programme

FEBRUARY 2024

ISTANBUL TECHNICAL UNIVERSITY ★ GRADUATE SCHOOL

LARGE SCALE WIRELESS PROPAGATION CHANNEL CHARACTERIZATION OF AIR-TO-AIR AND AIR-TO-GROUND DRONE COMMUNICATIONS

M.Sc. THESIS

Ubeydullah ERDEMİR
(504201352)

Department of Electronics and Communication Engineering

Telecommunication Engineering Programme

Thesis Advisor: Prof. Dr. Hakan Ali ÇIRPAN

FEBRUARY 2024

İSTANBUL TEKNİK ÜNİVERSİTESİ ★ LİSANSÜSTÜ EĞİTİM ENSTİTÜSÜ

HAVA-HAVA ve HAVA-YER DRONE HABERLEŞMESİ İÇİN BÜYÜK ÖLÇEKLİ KABLOSUZ YAYILIM KANALI KARAKTERİZASYONU

YÜKSEK LİSANS TEZİ

Ubeydullah ERDEMİR
(504201352)

Elektronik ve Haberleşme Mühendisliği Anabilim Dalı

Telekomünikasyon Mühendisliği Programı

Tez Danışmanı: Prof. Dr. Hakan Ali ÇIRPAN

ŞUBAT 2024

Ubeydullah ERDEMİR, a M.Sc. student of ITU Graduate School student ID 504201352 successfully defended the thesis entitled "LARGE SCALE WIRELESS PROPAGATION CHANNEL CHARACTERIZATION OF AIR-TO-AIR AND AIR-TO-GROUND DRONE COMMUNICATIONS", which he prepared after fulfilling the requirements specified in the associated legislations, before the jury whose signatures are below.

Thesis Advisor : **Prof. Dr. Hakan Ali ÇIRPAN** ....
Istanbul Technical University

Jury Members : **Dr. Ali GÖRÇİN** ....
Istanbul Technical University

Dr. İbrahim HÖKELEK ....
TÜBİTAK BİLGEM

Date of Submission : **05 January 2023**
Date of Defense : **20 February 2024**

To my dear spouse and children,

FOREWORD

I would like to express my sincere gratitude to my professors, Prof. Dr. Hakan Ali Çırpan and Dr. Ali Görçin, for their immense support, knowledge, and experience during my thesis work. They made this process meaningful and enjoyable, and I owe them an immeasurable debt of gratitude. I would also like to thank my esteemed colleague, Dr. İbrahim Hökelek, whose guidance and expertise were invaluable.

I am also grateful to my colleague Batuhan Kaplan, with whom I enjoyed working during my master's degree, and I believe will make significant contributions to the field. Additionally, I extend my thanks to the members of TÜBİTAK BİLGEM HİSAR Lab. for their generous support throughout my thesis work.

Lastly, I would like to express my endless gratitude to my dear family, whose unwavering support and presence have been a constant source of comfort and motivation throughout my life and particularly during this process.

February 2024

Ubeydullah ERDEMİR
(Electronics and Communication Engineer)

TABLE OF CONTENTS

ABBREVIATIONS

μ**s**	: Microsecond
5G	: Fifth-Generation
A2A	: Air–to–Air
A2G	: Air–to–Ground
CIR	: Channel Impulse Response
COTS	: Commercial Off-the-Shelf
dB	: Decibel
DPC	: Direct-path Component
DSP	: Digital Signal Processing
DSSS	: Direct Sequence Spread Spectrum
FE2R	: Flat-Earth Two-ray
FSPL	: Free Space Path Loss
GHz	: Gigahertz
Gbps	: Gigabit per second
GPSDO	: GPS Disciplined Oscillator
GS	: Ground Station
Hz	: Hertz
HAPS	: High Altitude Pseudo-Satellite
IQ	: In-phase and Quadrature-phase
LOS	: Line–of–Sight
MHz	: Megahertz
MPC	: Multipath Components
MIMO	: Multiple Input Mutliple Output
NF	: Noise Figure
NLOS	: Non–Line–of–Sight
OFDM	: Orthogonal Frequency Division Multiplexing
PAPR	: Peak-to-average Power Ratio
PDP	: Power Delay Profile
PL	: Path-Loss
PLE	: Path-Loss Exponent
PN	: Pseudorandom Noise
RFIC	: Radio Frequency Integrated Circuit
RMS	: Root-mean-square
RMS-DS	: RMS Delay Spread
RSS	: Received Signal Strength
RX-D	: Receiver Drone
SBC	: Single Board Computer
SDR	: Software-defined Radio
SISO	: Single Input Single Output

SoC : System on Chip
SRO : Sample Rate Offset
SSD : Solid State Drive
SWaP : Size Weight and Power
TX-D : Transmitter Drone
UAV : Unmanned Aerial Vehicle
WLAN : Wireless Local Area Network

SYMBOLS

$h(t,\tau)$	**:** Wireless communication channel
L	**:** Number of multipath components
$a_i(t)$	**:** Amplitude of the *i*–th multipath
$\phi_i(t)$	**:** Phase of the *i*–th multipath
$\tau_i(t)$	**:** Time delay of the *i*–th multipath
$\delta(\dot{})$	**:** Dirac delta function
η	**:** Path loss exponent
d_0	**:** Reference distance
ζ_{LS}	**:** Large scale characteristic losses
G_T	**:** Transmitter antenna gain
G_R	**:** Receiver antenna gain
λ	**:** Wavelength
h_T	**:** Transmitter antenna height
h_R	**:** Receiver antenna height
σ_τ	**:** RMS delay spread
$I_0(\cdot)$	**:** Zeroth-order modified Bessel function of the first kind
r_d	**:** Amplitude of the DPC

LIST OF TABLES

LIST OF FIGURES

LARGE SCALE WIRELESS PROPAGATION CHANNEL CHARACTERIZATION OF AIR-TO-AIR AND AIR-TO-GROUND DRONE COMMUNICATIONS

SUMMARY

Wireless communication is crucial in the information age. However, with the radio frequency spectrum becoming increasingly crowded, most devices operate in the "gold bands" of 300 MHz to 3 GHz. New standards offer faster broadband communication in higher frequency bands. Higher frequencies face limitations due to path loss, alignment problems, and atmospheric effects. Research labs and companies are striving to enhance communication techniques for the repeated use of present frequency bands. Some of the methods they are exploring include increasing channel capacity by using multiple antennas and intelligent surfaces that boost the power of transmitted signals at specific angles. However, these approaches require complex algorithms and location data, making them challenging to implement in practice. Vertical communication networks, including satellite, High-Altitude Pseudo-Satellite (HAPS), and Unmanned Aerial Vehicle (UAV) platforms, are being studied to increase network capacity and diversification. Satellite communication is a mature technology with uninterrupted global coverage but limited capacity and latency due to high altitude. HAPS systems are an alternative to satellites and offer wide coverage areas. They fly at an altitude between 20 to 50 km, providing communication services for weeks to months. HAPS systems have low latency and high channel capacity, but the technology is still under development. UAV platforms are an alternative option to consider. They come in various sizes and can be easily deployed to provide high-bandwidth communication services to small areas. Although they have shorter flight times and lower altitudes compared to other platforms, recent studies have shown that the significance of these limitations is decreasing. UAVs can provide dynamic coverage services in areas where cellular communication networks have difficulty providing coverage, such as blind spots and rural areas with no network.

This study investigates the use of UAVs to enhance existing and future cellular communication systems. While there has been extensive research on UAV channels, there is a lack of studies on to use of UAVs in cellular communication. The purpose of this thesis is to fill this gap in the literature. Studies on channel measurement have been conducted using commercial systems or specially designed structures consisting of signal generators and analyzers. However, there is a need for a light and low-power channel measurement system that can be mounted on UAV platforms. The existing Software-defined radio (SDR) hardware is analyzed for suitability, and laboratory measurements are carried out. The hardware components are made suitable for flight. Transmitter SDRs are configured using manufacturer software libraries. Signals are generated, captured, processed, and stored on the receiver side. Calibrations are carried out after system stability is confirmed with flight tests. Relevant

calibration data are applied to the measurement outputs to eliminate system-related static disturbances. The channel measurement system has three subsystems: antenna, SDR, and mechanical. Omnidirectional antennas are designed and manufactured for specific frequency bands. Six antennas have been produced, and their radiation patterns are obtained through simulation. The design of Analog Devices' Radio Frequency Integrated Circuit (RFIC)-based receiver/transmitter is examined in the SDR subsystem. Solutions to the high-speed interface problem for broadband channel measurement are explained. Solutions to problems encountered in the encapsulation of the measurement system and the UAVs used are shared in the mechanical subsystem.

In Chapter 3, the signal processing algorithms that run on the measurement results are included. As mentioned before, the information received from the UAV and the channel measurement system is recorded in the local memory. At this point, the outputs of the channel measurement system and UAV flight data records are evaluated separately. Raw airborne IQ data first enters the autocorrelation function with the PN sequence broadcast from the transmitter. After the intermediate processes, the peak estimation of the first and strongest incoming signal is made through the Power Delay Profile (PDP) obtained. To reduce the computational load, a certain period of time (e.g. 10 μs) is taken from the peak value. Additionally, the power of the resulting peak is calculated and accumulated for use in narrowband modeling. While Root-Mean-Square Delay spread (RMS-DS), Ricean K-factor, and PDP analyses are performed on the processed PDP, the power value is used to analyze it together with path loss models. In order to evaluate the suitability of the channel measurement system for measurements and to remove system-related fixed errors from the measurement results, calibrations were carried out by connecting the transmitter to the receiver via a known cable channel. Here, it is first necessary to convert the relative power value read into absolute power value. A cable channel consisting of attenuators and long cables, whose loss has been previously measured, is connected between the transmitter and the receiver. The power value obtained after the correlation process at the receiver is multiplied by a constant to equalize the measured value. This value is then used as the power calibration coefficient in measurements at the relevant frequency. Since there is no multipath in the cable channel, no signal other than the main signal is expected to be seen in the PDP analysis. As a result of the calibration measurements, no signal was observed up to approximately 70 dB below the main signal. This indicates that there will be no system-related component in the system's broadband measurements. Similarly, RMS-DS calibration measurements show a constant value. This value was reset to zero and used as the calibration value in the measurements.

Finally, Chapter 4 is on the performed measurements. First, the measurement environment is discussed in detail. The parameters of the flights performed and the images taken during the measurement are given. The UAV carrying the transmitter payload followed the same route autonomously in all measurements. In each measurement, the UAV lands on the ground, changes batteries, and flies again for the next measurement. The receiver is placed on the mast available on the vehicle in Air–to–Ground (A2G), and measurements are taken. In each measurement, the antenna belonging to the frequency band to be measured is mounted on the mast. During this period, the mast height is constant. In air-to-air measurements,

measurements are taken by flying the receiver payload on a second UAV. Following the completion of the measurement, the receiver UAV was lowered to the ground. Air-to-ground measurements were taken at 1750, 2560, and 3500 MHz frequencies, and air-to-air measurements were taken at 3500 MHz frequency. Afterward, antenna polarization and orientation are explained in detail. Measurement results were evaluated in path loss models, PDP, RMS-DS, and Ricean K-factor analyses. In the path loss models section, A2G measurements have a very similar increase slope with the Free–space path loss (FSPL) model. In addition, the important point that stands out in these measurements is that the measurements taken have high compatibility with the flat-earth two-ray (FE2R) model. In air-to-air measurements, although results close to the FSPL model are obtained, there is a significant fluctuation that varies randomly depending on the distance. In the PDP analysis, it is noteworthy that the reflections in the channel occur and disappear at different delays depending on the distance. Although reflections generally occur at levels close to the main signal in A2G measurements, distant and strong reflections may also occur. In Air–to–Air (A2A) measurements, reflections are distributed more homogeneously over time. As in A2G measurements, strong reflections due to land features are observed. For both scenarios, the source of these reflections was tried to be determined geometrically, and verification was made from the delays on the received PDP. Another point worth noting here is that the main signal can be separated from the strong reflection coming from the ground up to a certain distance. Finally, RMS-DS and Ricean K-factors were examined. The distant and strong reflections occurring in the previously mentioned channel increased the RMS-DS parameters in A2G measurements to much higher values than their average value for a short time. In A2A measurement, since the reflections occurred homogeneously, the RMS-DS value increased as the distance increased, and after a point, it scattered around the mean value. Although Ricean K-factors are in a trend following the RMS-DS parameter, they differ at some points. For example, in air-air measurements, since there was almost no strong reflection at the beginning of the measurement, it took very high values, and as the effect of reflections increased, it scattered around a constant value such as the RMS-DS parameter.

Although UAV channels have been examined comprehensively, there are many points that need to be improved. Taking measurements in regions with different terrain characteristics (cities, mountainous areas, sea surface, etc.) according to usage scenarios such as applications requiring high data rates, high reliability, low latency is considered an important study about UAV channels. In addition, it is important to make measurements and analyzes in the frequency bands planned to be used in the future, in addition to the currently used cellular communication frequency bands. In addition, measurements should be targeted in frequency bands that can be used for different applications other than cellular communication. Finally, the designed channel measurement system works in the SISO structure. In future studies, analog and digital blocks that can operate in multiple antenna structures can be added to the channel measurement system.

HAVA-HAVA ve HAVA-YER DRONE HABERLEŞMESİ İÇİN BÜYÜK ÖLÇEKLİ KABLOSUZ YAYILIM KANALI KARAKTERİZASYONU

ÖZET

Bilgi çağında kablosuz iletişim giderek daha hayati bir önem kazanmaktadır. Yeni geliştirilen cihazlar çok sayıda kablosuz bağlantı arayüzü sunmaktadır. Bu durum radyo frekans spektrumunda giderek daha kalabalık bir ortam haline getirmektedir. Yeni nesil haberleşme standartları daha hızlı, dolayısıyla daha genişbant haberleşme sistemlerini adreslemektedir. Mevcut kullanılan cihazların çoğunun "altın bantlar" olarak adlandırılan 300 MHz - 3 GHz arasında çalıştığı göz önüne alınırsa yeni teknolojiler daha yüksek frekanslarda çalışmak durumundadır. Her ne kadar spektrum çok geniş olsa da yol kaybı, hizalama kaynaklı sıkıntılar ve atmosfer kaynaklı etkiler 3 GHz ve üzeri bantların kullanımını sınırlandırmaktadır.

Öte yandan araştırma enstitüleri ve şirketler daha etkili ve verimli iletişim teknikleri kullanarak mevcut bantların tekrar tekrar kullanımının önünü açmak için yarışmaktadır. Bunun sonucu olarak çoklu anten yapıları ve akıllı yüzeyler kullanarak kanal kapasitesi artırılmaya çalışılmaktadır. Çoklu anten yapıları ile hüzme yönlendirme algoritmaları kullanılarak yol kaybına karşı iletilen sinyalin gücü alıcıda artırılmaya çalışılmaktadır. Öte yandan akıllı yansıtıcı yüzeyler kullanılarak haberleşme kanalına müdahale edilerek gönderilen sinyallerin istenilen açılarda yansıtılarak alıcıya daha güçlü bir şekilde ulaştırılmaya çalışılmaktadır. Her iki teknikte de karmaşık kanal kestirim algoritmaları ve alıcının konum bilgisi kullanılmaktadır. Bu durum, pratikte karmaşıklığı önemli ölçüde artırmaktadır.

Tüm bu tekniklerin yanı sıra eskiden beri üzerinde çalışılan bir konu da dikey haberleşme ağlarıdır. uydu, yüksek irtifa sözde uydu (high-altitude pseudo-satellite, HAPS) ve insansız hava aracı (İHA) platformlarının iletişim ağlarına dahil olduğu dikey ağlar güncel araştırma konuları arasında yer almaktadır. Buradaki temel motivasyon, karasal iletişim kanallarının karmaşıklığının dikey ağlarda söz konusu olmamasıdır. Daha basit haberleşme kanalları ile istenilen çeşitleme ve kapasite artışı kolaylıkla ulaşılabilmektedir. Öncelikle uydu haberleşme teknolojileri, yıllardır kullanımda olan olgun bir teknolojidir. Tüm dünya üzerinde kesintisiz bir kapsama sunmaktadır. Bu da hücresel haberleşmeye uygun bir alternatif olarak öne çıkmaktadır. Ancak hizmet sunduğu alanın genişliği ve uyduların çok yüksek irtifalarda olması sebebiyle sağlanabilecek kapasite ve düşük gecikme isterleri sınırlanmaktadır.

Bu noktada alternatif platformlar ön plana çıkmaktadır. HAPS sistemleri, uydu kadar olmasa da çok geniş bir kapsama alanı sunmaktadır. Bu sistemlerin hedeflenen irtifaları, normal havayolu trafiğinin üzerinde, 20 ila 50 km seviyelerindedir. Haftalarca ve hatta aylarca sabit bir noktada uçarak geniş bir alana haberleşme hizmeti verilmesi hedeflenmektedir. Her ne kadar kapsama alanı, kanal kapasitesi ve düşük

gecikme noktasında optimum çözüm olarak görülse de pratikte platform teknolojisi henüz geliştirilme aşamasındadır.

Bir başka alternatif ise İHA platformlarıdır. Her ne kadar İHA denilince akla birkaç kilogram ağırlığında ve düşük faydalı yük kapasitesine sahip ticari İHA'lar gelse de her boyut ve ağırlıkta İHA platformu bulmak mümkündür. İHA platformları diğer dikey ağ platformlarından belli noktalarda ayrılmaktadır. Avantajları kolaylıkla konuşlandırılabilmeleri ve istenilen küçük bölgelere yüksek bant genişlikli haberleşme hizmeti sunabilmeleridir. Dezavantajları ise diğer platformlara göre kısa uçuş süreleri ve düşük irtifalarıdır. Ancak güncel çalışmalarla bu sınırlamalar giderek daha az önemli hale gelmektedir. Hücresel haberleşme ağlarının kapsamakta zorlandığı kör noktalarda ve herhangi bir ağın bulunmadığı kırsal alanlarda İHA'lar kullanılarak dinamik bir kapsama hizmeti sağlanabilmektedir.

Bu çalışmada, yeni nesil hücresel haberleşme sistemlerine destek olacak şekilde İHA kullanımı çalışmalarına katkı sağlanması hedeflenmiştir. Bunun için öncelikle üzerinde çalışılan kanalın özelliklerinin bilinmesi gerekir. İHA kanalları, hava araçları için yeni nesil haberleşme sistemleri, WLAN tabanlı İHA haberleşme sistemleri gibi çeşitli uygulamalar için literatürde detaylıca incelenmiştir. Ancak İHA'ların kullanım senaryoları içerisinde önemli bir yer tutan hücresel haberleşmeye destek olacak şekilde kullanımlar için yeterli çalışma mevcut değildir. Bu tez çalışmasında literatürdeki bu boşluğun giderilmesine katkı sağlanmıştır.

Literatürde mevcut kanal ölçüm çalışmaları, rafta hazır ticari sistemler veya özel tasarlanmış sinyal üreteci ve analizörlerinden oluşan özel tasarım yapılarla gerçekleştirilmiştir. Bu noktada hedeflenen çalışma için esneklik sağlamak amacıyla İHA platformlarına takılabilecek kadar hafif ve düşük güç tüketen bir kanal ölçüm sistemi gereksinimi doğmuştur. Bu hususta gerçekleştirilen çalışmalar 2. ve 3. bölümlerde detaylıca ele alınmıştır. İlk olarak mevcut yazılım tanımlı radyo (software defined radio, SDR) donanımlarının bu iş için uygun olup olmadığı analiz edilmiş ve laboratuvar ölçümleri gerçekleştirilmiştir. Burada önemli olan nokta alıcı ve verici arasında frekans senkronizasyonunun olması ve ölçüm boyunca senkron kalmalarını sağlamaktır. Daha sonra diğer donanımlar da uçuş için uygun hale getirilip kutulanmıştır. Cihazlar arasındaki elektromanyetik girişim, titreşim gibi sistem seviyesinde karşılaşılan bazı donanımsal problemler de önce tespit edilip daha sonra çözülmeye çalışılmıştır. Yazılım geliştirme kısmında ise SDR donanımının üreticisi tarafından sağlanan kütüphaneler kullanılarak verici SDR'ların konfigürasyonu yapılmış ve verici tarafında sinyal üretilip gönderilmiş, alıcı tarafında ise bu sinyaller yakalanıp işlenerek saklanmıştır. Ayrıca alıcı kısmında ek kontrol amaçlı kodlar eklenmiştir. Tüm bu aşamaların sonunda sistem kararlılığı uçuşlu testlerle birlikte doğrulandıktan sonra kalibrasyon faaliyetleri icra edilmiştir. Ölçümler gerçekleştirilmeden önce ilgili kalibrasyon verileri alınmış, ölçüm çıktıları üzerine uygulanarak sistem kaynaklı statik bozucu etkiler giderilmiştir.

Kanal ölçüm sisteminin anten, SDR ve mekanik altsistemleri mevcuttur. Anten altsisteminde ölçüm yapılacak frekans bantlarına özel eşyönlü antenler tasarlanıp üretilmiştir. üç ayrı frekans bandı için toplamda 6 adet anten üretilmiştir. Bu antenlerin benzetim yoluyla ışıma desenleri hesaplanmış, daha sonra ölçümlerin analizlerinde kullanılmıştır. SDR altsisteminde ise Analog Devices firması tarafından üretilen

AD9361 radyo frekans entegre devre (radio frequency integrated circuit, RFIC) tabanlı alıcı/verici tasarımında göz önünde bulundurulması gereken noktalar incelenmiş, bu noktalara sunulan çözümler anlatılmıştır. Genişbant kanal ölçümü yapılabilmesi için yüksek hızlı arayüzler kullanılması gerekmektedir. Mevcut cihazlarda bu isterin nasıl çözüldüğünden detaylıca bahsedilmiştir. Mekanik altsisteminde ise kanal ölçüm sisteminin kutulanmasında karşılaşılan problemlerin çözümlerinden ve kullanılan İHA'lar hakkında bilgiler paylaşılmıştır.

3. Bölümde, ölçüm sonuçlarının üzerinde çalıştırılan sinyal işleme algoritmalarına yer verilmiştir. İHA ve kanal ölçüm sisteminden alınan bilgiler daha önceden de bahsedildiği gibi yerel hafızaya kaydedilmektedir. BU noktada kanal ölçüm sisteminin çıktıları ile İHA uçuş verisi kayıtları ayrı şekilde değerlendirilmektedir. Havadan yakalanan ham IQ verileri ilk olarak vericiden yayınlanan PN dizisi ile özilişki işlevine girer. Ara işlemlerden sonra elde edilen PDP üzerinden ilk ve en güçlü gelen sinyalin tepe kestirimi yapılır. İşlemsel yükü azaltmak için tepe değerinden belirli bir süreye kadarlık kısmı (örneğin 10 μs) alınır. Ayrıca elde edilen tepe noktasının gücü hesaplanır ve darbant modellemelerde kullanılmak üzere biriktirilir. İşlenmiş PDP üzerinden RMS-DS, Ricean K-faktörü ve PDP analizleri gerçekleştirilirken güç değeri kullanılarak yol kaybı modelleri ile beraber analizi yapılır.

Kanal ölçüm sisteminin ölçümlere uygunluğunu değerlendirmek ve sistem kaynaklı sabit hataları ölçüm sonuçlarından çıkarmak üzere verici, alıcıya arada bilinen bir kablo kanalı ile bağlanarak kalibrasyonlar gerçekleştirilmiştir. Burada öncelikli olarak okunan göreli güç değerini, mutlak güç değerine dönüştürmek gerekir. Verici ile alıcı arasına sönümleyiciler ve uzun kablolardan oluşan, daha önceden kaybı ölçülmüş bir kablo kanalı bağlanmıştır. Alıcıda korelasyon işlemi sonrasında elde edilen güç değeri, ölçülen değere eşitlenmesi için bir sabit ile çarpılır. Bu değer daha sonra ilgili frekanstaki ölçümlerde güç kalibrasyon katsayısı olarak kullanılmaktadır. Kablo kanalında herhangi bir çokyol mevcut olmadığından PDP analizinde ana sinyal dışında bir sinyal görülmesi beklenmemektedir. Yapılan kalibrasyon ölçümleri sonucunda ana sinyalden yaklaşık 70 dB aşağısına kadar herhangi bir sinyal görülmemiştir. Bu da sistemin genişbant ölçümlerinde, sistem kaynaklı bir bileşenin bulunmayacağına işaret etmektedir. Benzer şekilde RMS-DS kalibrasyon ölçümlerinde de sabit bir değer gelmektedir. Bu değer sıfırlanarak, ölçümlerde kalibrasyon değeri olarak kullanılmıştır.

Son olarak 4. Bölüm gerçekleştilen ölçümler üzerinedir. İlk olarak ölçüm ortamı detaylı olarak ele alınmıştır. Gerçekleştirilen uçuşların parametreleri ve ölçüm sırasında alınmış görseller verilmiştir. Verici faydalı yükünü taşıyan İHA, tüm ölçümlerde otonom olarak aynı rotayı takip etmiştir. Her ölçümde İHA yere inmiş, bataryaları değiştirildikten sonra bir sonraki ölçüm için tekrar yükselmiştir. Alıcı ise Havadan yere yapılan ölçümlerde araç üzerinde mevcut olan masta yerleştirilerek ölçümler alınmıştır. Her ölçümde, ölçüm yapılacak frekans bandına ait anten mast üzerine takılmıştır. Bu süre zarfında mast yüksekliği sabittir. Havadan havaya yapılan ölçümlerde ise alıcı faydalı yükü ikinci bir İHA üzerinde uçurularak ölçümler alınmıştır. Ölçümün tamamlanmasına müteakip alıcı İHA yere indirilmiştir. 1750, 2560 ve 3500 MHz frekanslarında Hava-Yer, 3500 MHz frekansında Hava-Hava ölçümleri alınmıştır. Daha sonrasında anten polarizasyonu ve yönelimi detaylı olarak açıklanmıştır.

Ölçüm sonuçları, yol kaybı modelleri, PDP, RMS-DS ve Ricean K-faktörü analizlerinde değerlendirilmiştir. Yol kaybı modelleri kısmında havadan yere yapılan ölçümler serbest uzay yol kaybı (free space path loss, FSPL) modeliyle çok yakın bir artış eğimine sahiptir. Ayrıca bu ölçümlerde önemli bir şekilde dikkat çeken nokta, alınan ölçümlerin düz dünya iki yol (flat earth two ray, FE2R) modeli ile yüksek uyumluluğa sahip olmasıdır. Hava-hava ölçümlerinde ise FSPL modeline yakın sonuçlar elde edilmesine karşın mesafeye göre rastgele değişen belirgin bir dalgalanma mevcuttur. PDP analizinde, kanalda oluşan yansımaların mesafeye göre farklı gecikmelerde oluşumları ve kaybolmaları dikkat çekmektedir. Hava-Yer ölçümlerinde yansımalar genellikle ana sinyale yakın seviyelerde oluşmasına karşın uzak ve güçlü yansımalar da oluşabilmektedir. Hava-Hava ölçümlerinde ise yansımalar daha homojen bir şekilde zamana dağılmaktadır. Hava-Yer ölçümlerinde olduğu gibi arazi özellikleri kaynaklı güçlü yansımalar görülmektedir. Her iki senaryo için bu yansımaların kaynağı geometrik olarak tespit edilmeye çalışılmış, alınan PDP üzerindeki gecikmelerden doğrulama yapılmıştır. Burada dikkat çeken bir diğer nokta da ana sinyalin yerden gelen güçlü yansımadan belirli bir mesafeye kadar ayrışabildiği gözlenmektedir. Son olarak RMS-DS ve Ricean K-faktörleri incelenmiştir. Daha önceden de bahsi geçen kanalda oluşan uzak ve güçlü yansımalar hava-yer ölçümlerinde RMS-DS parametrelerini kısa süreliğine ortalama değerinden çok daha yüksek değerlere çıkarmıştır. Hava-hava ölçümünde ise yansımalar homojen bir şekilde oluştuğundan mesafe arttıkça RMS-DS değeri artmış, bir noktadan sonra sabit bir değer etrafında saçılmıştır. Ricean K-faktörleri ise RMS-DS parametresini takip eden bir trend içinde olmasına karşın bazı noktalarda ayrışmaktadır. Örneğin hava-hava ölçümlerinde ölçümün başlarında neredeyse hiç güçlü bir yansıma oluşmadığından çok yüksek değerler almış, yansımaların etkisi arttıkça, RMS-DS parametresi gibi bir sabit değer etrafında saçılmıştır.

Her ne kadar kapsamlı bir şekilde İHA kanalları irdelenmiş olsa da geliştirilmesi gereken bir çok nokta mevcuttur. Yüksek veri hızları, yüksek güvenilirlik, düşük gecikme gerektiren uygulamalar gibi kullanım senaryolarına göre farklı arazi özelliklerine sahip bölgelerde (şehirler, dağlık alanlar, deniz yüzeyi vb.) ölçümlerin alınması İHA kanalları hakkında önemli bir çalışma olarak görülmektedir. Ayrıca halihazırda kullanılan hücresel iletişim frekans bantları dışında, gelecekte kullanılması planlanan frekans bantlarında da ölçüm ve analizlerin yapılması önem arzetmektedir. Ayrıca hücresel haberleşme dışında farklı uygulamalar için kullanılabilecek frekans bantlarında da ölçümler hedeflenmelidir. Son olarak tasarlanan kanal ölçüm sistemi SISO yapısında çalışmaktadır. Gelecek çalışmalarda çoklu anten yapılarında çalışabilen analog ve dijital bloklar kanal ölçüm sistemine eklenebilir.

1. INTRODUCTION

Unmanned Aerial Vehicles (UAVs), also known as drones, have seen an exponential growth in usage in recent years, with their applications ranging from cargo transportation, smart agriculture, surveillance, public safety, disaster management, science, and military operations [1]–[3]. High-speed wireless communication is critical for all of these applications, as they require the transfer of high-quality images and videos from one drone to another or to the ground station (GS). The integration of terrestrial and non-terrestrial systems, such as UAVs and satellites, is a highly popular topic in the development of 5G and beyond networks. The integration of UAVs into these networks has the potential to increase connectivity and coverage of remote areas. To ensure the successful and reliable operation of UAVs, it is essential to accurately characterize the wideband wireless communication channel for A2G and A2A communication operating at 5G carrier frequencies. This will help in designing reliable waveforms for these environments by ensuring that communication is robust and reliable across different environments and conditions, such as in urban, suburban, and rural areas, under various weather conditions, and in the presence of potential electromagnetic interference. By characterizing the wireless communication channel, the design of UAV communication systems can be optimized to ensure that they meet the requirements of their intended applications, and help to enhance the safety, efficiency, and effectiveness of UAV operations.

1.1 Related Works on Drone Channel Measurements

A comprehensive survey of the A2G channel models for UAVs have been provided in [4]–[6], where the primary distinction of the UAV A2G channels is the addition of a third dimension as an altitude. The important parameters include the type of channel sounding signal, its center frequency, bandwidth, transmit power, UAV speed, heights of UAV and GS, link distance, elevation angle, and local GS environment characteristics.

Channel measurements for A2G channels are given in [7]. The measurements are done with a specifically designed channel sounder with a peak-to-average power ratio (PAPR)-optimized multitone signal with 10 MHz bandwidth. Measurements were conducted at 970 MHz, and the flight route has a maximum range of about 400 km. The results of this study give power-delay profile (PDP) and heatmap of multipaths. The study in [8] shows how ground reflections affect the signal strength in the L-band air-to-ground channel. It shows both theoretical and experimental results from the previous study and uses a two-ray model to explain the signal variation. It also notes that the signal variation is often less than expected because the ground reflections are weak or blocked by obstacles. The studies in [9]–[12] examine a wide range of measurements. The system uses a sounder with the transmitting side on the ground and the receiving side on the aircraft. The sounding signals are transmitted in dual bands, 5 MHz in the L-band (968 MHz) and 50 MHz in the C-band (5080 MHz). The receiver has two receiving channels for each frequency band, for a total of 4 receiving channels. CIR is obtained from the received signals and analyzed for PDP, log-distance PL, RMS-DS, Ricean-K Factor, and TDL over sea [9], mountainous [10] and rural/urban areas [11]. The shadowing effect of the airplane was also analyzed at [12]. In another recent study [13], the authors characterize A2G wireless channels for L-Band (1-2 GHz) and C-Band (4-8 GHz) using a commercially available drone equipped with software-defined radio (SDR). The drone is used to transmit wideband chirp waveforms whose bandwidths are 26 MHz and 48 MHz for L-band and C-band, respectively, while a commercial signal and spectrum analyzer on the ground is used as the receiver. The measurement-based models for path loss exponents and shadowing for the radio channel between UAVs and live LTE networks operating at the carrier frequency of 800 MHz are studied in [14]. The authors identify that the height of UAV is an important parameter for characterizing the propagation channel for UAVs as the average number of detected cells increases as the UAV moves higher altitudes. In [15,16], A2G channel measurements were performed with COTS equipment using various 802.11 radio standards. These measurements are based on received signal strength (RSS) information about the channel. A modem with 2 antennas was used in the air segment, while an AP with 2 antennas was used in the ground segment. In [17] MIMO channels between UAV and ground are analyzed. Measurements were performed at 915 MHz. Two antennas mounted on the drone were transmitted sounding signals and on the ground, these signals were received with a linear array of 8 antennas. The signal used is DSSS signals with a bandwidth of 10 MHz. The measurements were analyzed comprehensively and PDP, RMS-DS and spatial diversity were analyzed over the obtained CIR. In [18], the effects of a human body on the A2G channel model are studied through measurement experiments when the UAV is at low altitudes while there are three different use cases of holding user equipment, namely, near-chest facing, in-pocket facing, and near-chest facing-away. The article [19] provides a detailed overview of recent studies in the A2A channel measurements. The number of measurement-based channel characterization studies for A2A wideband wireless communication channels is limited compared to the A2G studies. A preliminary effort in this field is given in [20]. In this study, using a 20 MHz signal at a center frequency of 250 MHz, the channels between 2 Cessna aircraft in the air were measured at different combinations of altitude and land cover. The RUSK channel sounder [21], which is manufactured by Medav GmbH, was used for the measurements. The PDP and Doppler spread parameters of the measured channel were emphasized. As a continuation of this study, [22] and [23] studies were conducted. In these studies, the measurements taken in the same band were statistically analyzed. Noting that in [23], it was found that the strength of the main component in the channel fits very well with the Ricean distribution. The study in [24] investigates the radio propagation characteristics of A2A links for unmanned aircraft services (UASs) in disaster recovery scenarios. The authors employ two small manned airplanes and a 20-MHz bandwidth OFDM signal at 2.3 GHz to measure the channel impulse responses (CIRs) in various environments. They observe that ground reflection affects the CIR when flying over the sea, but not over urban areas due to the presence of tall buildings. The studies [25,26] aim to provide detailed knowledge about the propagation channel for A2A drone communications with IEEE 802.11 standard's frequencies. In the first study, the authors conduct field experiments to characterize the

A2A channel for an 802.11-based low-altitude network using UAVs. They propose a modified model to describe the propagation path loss and show the simulation results of the A2A channel characteristics. The second study focuses on estimating the path loss exponent (PLE) for line–of–sight (LOS) A2A drone communications by investigating the large-scale channel propagation statistics. While the first study examines the small-scale channel characteristics and multi-path effect, the second study looks at the path loss model and large-scale channel statistics. Channel measurements for A2A were conducted at 5.2 GHz with 100 MHz bandwidth in urban environments in [27]. To transmit the channel sounding signal for characterizing the propagation effects, analog optical links were utilized. The exact trajectories of the drones, along with the three-dimensional layout of the environment, were used in these measurements. In [28], as an extension study, the authors performed the same measurement campaign for several flight paths in three different environments to establish a relationship between the real-world objects and the multipath components. In [29], field experiments were conducted to measure the effects of mobility uncertainties on mmWave/THz-band communications between drones. The findings were then utilized to perform capacity analysis based on simulations.

1.2 Contribution

The contributions of the studies carried out in the thesis are summarized:

- Field measurements in the literature have typically focused on the frequencies used in the 802.11 standards, specifically 2.4 and 5 GHz when performed with COTS hardware. On the other hand, when performed with dedicated hardware, a target application such as L-band Digital Aeronautical Communications System (LDACS) is considered [30]. In this study, since the use of drones to improve cellular communication is examined, it is observed that there are not enough field studies in the literature to model the wireless channels of UAVs. In our field studies, measurements were taken and analyzed in cellular communication bands.

- A lightweight channel sounder that can be attached to the drone and that operates with high enough consistency to perform broadband channel measurements has been developed.
- Since the number of A2A measurements in the literature is limited, and most measurements are not wideband, this study aims to make an important contribution to A2A broadband measurements.
- In the literature, A2A measurements have been performed either at very high altitudes, as high as airlines, or very close to the ground. Practically, UAV flight altitudes are in between these two altitudes. In this study, UAV channels were performed at an altitude of 100 meters.
- Multiple field measurements were taken on the same flight route at various frequencies for easier analysis of frequency changes.

This thesis presents a field measurement-based channel characterization for wireless communication systems that operate in the A2G and A2A scenarios. The characterization is done using two DJI Matrice 600 Pro drones equipped with lightweight SDRs. Measuring the wireless communication channels in A2G and A2A scenarios is a challenging task. It requires transmitting and receiving high-speed data at the transceiver and storing a massive amount of data at the receiver. The weight limit of the payload that can be carried by a drone makes it difficult to use conventional transceivers. Therefore, we employed cost-effective and lightweight SDR-based transceivers for transmitting and receiving radio signals over the air. To generate and store high data rate baseband IQ samples, we used a single board computer (SBC) with solid state drive (SSD). We ensured precise frequency synchronization between the transmitting and receiving SDRs using a GPS disciplined oscillator (GPSDO). The GPS receiver provided high-precision location measurements of both the transmitting and receiving drones, which were remotely controlled through a WLAN interface operating at a carrier frequency of 915 MHz. We used this control interface to manage the experiments by starting and stopping the measurements. In this study, we employed a correlation-based channel sounder. The transmitting drone broadcasted a sounding waveform consisting of a pseudo–noise (PN)–sequence with a length of 4095, and the receiving drone captured the sounding waveform along with the location information for post-processing analysis.

The path loss results of the measurements, log-distance PL model, FSPL and FE2R models for the A2G and A2A scenarios demonstrate that the measurement and FE2R results have similar trends for A2G while the measurement and FSPL are similar to each other for A2G. The time delay between direct path and multipath components mostly lies between 0 and 300 ns for A2G while it is widely spread between 0 and 150 ns for A2A. There are several buildings having metal roofs and claddings on the measurement site, where the reflections from these structures result in sudden peaks in the RMS-DS. The results indicate that the A2A channel has better characteristics than the A2G under similar mobility conditions indicating that higher capacities can be achieved by the A2A scenario using the same bandwidth.

1.3 Theoretical Background

In this thesis, wireless channels for both A2G and A2A are examined using the field measurements. To define the wireless propagation channel with multipath fading as a time-variant system, the same model is used for both A2G and A2A channels. The wireless channel containing multipath components is expressed as

$$h(t,\tau) = \sum_{i=0}^{L-1} a_i(t) \mathrm{e}^{j\phi_i(t)} \delta(\tau - \tau_i(t)) \tag{1.1}$$

where L refers to the number of channel taps, and $a_i(t)$, $\phi_i(t)$, and $\tau_i(t)$ represent the amplitude, phase, and delay of the i–th path, respectively.

For narrowband modeling, an important measure that we consider is the log-distance path-loss (PL) model [31], which characterizes the received power with respect to the distance between a transmitter and a receiver. It is expressed as

$$\mathrm{PL}(d) = \underbrace{20 \log \frac{4\pi d_0}{\lambda}}_{\mathrm{PL}_0} + 10\eta \log(d/d_0) + \zeta_{LS}, \tag{1.2}$$

where d is the distance between a transmitter and a receiver in meters, η is the PLE, d_0 is the reference distance for path loss measurements, PL_0 is the path loss at reference distance, and ζ_{LS} contains remaining large–scale characteristic losses such as shadowing. On the other hand, although the log-distance PL model provides sufficient information about the wireless propagation channel, in most cases, a more accurate model is needed. In this case, the FE2R model given in [32], where the ground reflection is also considered, is employed. It is calculated as

$$FE2R(d) = -10\log\left(\underbrace{4G_\mathrm{T}G_\mathrm{R}\left(\frac{\lambda}{4\pi d}\right)^2}_{\text{FSPL}}\sin^2\left(\frac{2\pi h_\mathrm{T} h_\mathrm{R}}{\lambda d}\right)\right) \tag{1.3}$$

where G_T and G_R are antenna gains, λ is the wavelength, h_T and h_R are the heights of transmitter and receiver antenna and d is the distance between transmitter and receiver antennas.

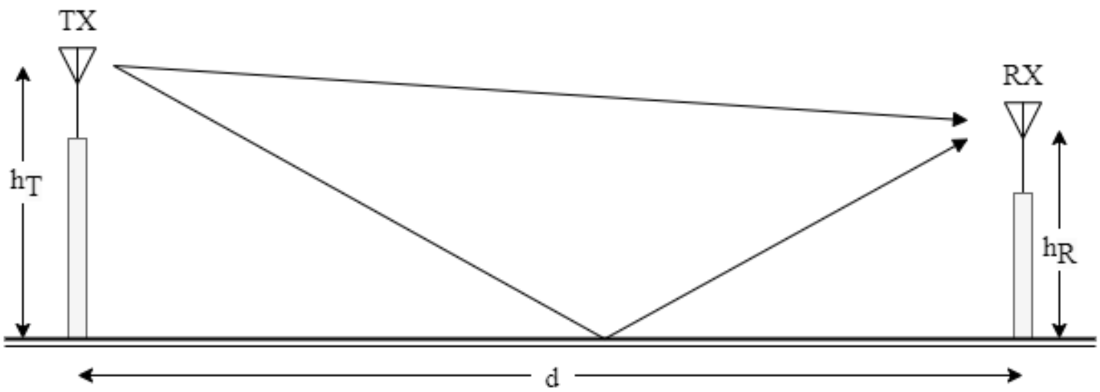

Figure 1.1 : Flat earth ground reflection.

Considering the wideband modeling, both the strength and arrival time of the reflections in the channel are analyzed. At this point, PDP is an important analysis method to understand the characteristics of the channel. Specifically, the instantaneous PDP is obtained by

$$S(t,\tau) = |h(t,\tau)|^2 \tag{1.4}$$

where, $h(t,\tau)$ represents the CIR. With this metric, it is possible to analyze the power level, formation, and disappearance times of each reflection that arrives at the receiver at different times from the channel. Also, RMS-DS is an important metric that provides information about the multipath richness of the channel. The mathematical form of RMS-DS given in [31] is the second-order central moment of the PDP. It is calculated as

$$\sigma_\tau = \sqrt{\frac{\sum_{k=0}^{L-1} a_k^2 \tau_k^2}{\sum_{k=0}^{L-1} a_k^2} - \left(\frac{\sum_{k=0}^{L-1} a_k^2 \tau_k}{\sum_{k=0}^{L-1} a_k^2}\right)^2} \tag{1.5}$$

where σ_τ is the RMS delay spread for an instantaneous link distance. The RMS-DS parameter plays an important role in the deciding design parameters of the communication systems.

The statistical modeling of the channel is performed based on the Rician distribution. Its mathematical form is given in [32]

$$p(r) = \frac{r}{\sigma^2} \exp\left(-\frac{r^2 + r_d^2}{2\sigma^2}\right) I_0\left(\frac{r r_d}{\sigma^2}\right) \tag{1.6}$$

where r is received signal amplitude, r_d denotes the amplitude of direct-path component (DPC) and σ^2 is the total power of the MPC. Also, $I_0(\cdot)$ is the zeroth-order modified Bessel function of the first kind. The Ricean distribution is typically characterized by the K parameter. This parameter is defined as

$$K(dB) = 10log(\frac{r_d}{2\sigma^2}). \tag{1.7}$$

The parameter K expresses the power of the DPC and the total power of the MPC in dB. If $K \to 0$, the distribution approaches to Rayleigh distribution. On the other hand, if K is greater than one, it becomes Gaussian with a mean value of r_d. It gives a powerful insight into the variation of the received power and, implicitly, the reliability of the channel.

2. MEASUREMENT SYSTEM

2.1 System Overview

For our channel measurements, TUBITAK BILGEM has sponsored the development of an SDR-based, highly tunable single input single output(SISO) channel sounder and antennas. Basically, It is a direct sequence spread spectrum (DSSS) correlator. The transmitter has a wideband power amplifier (PA), and the receiver utilizes also a wideband low-noise amplifier (LNA). For each measurement in desired frequency band, the transmitter and the receiver are both tune in the desired measurement frequency. The channel sounder high-level system model is shown in Fig. 2.1.

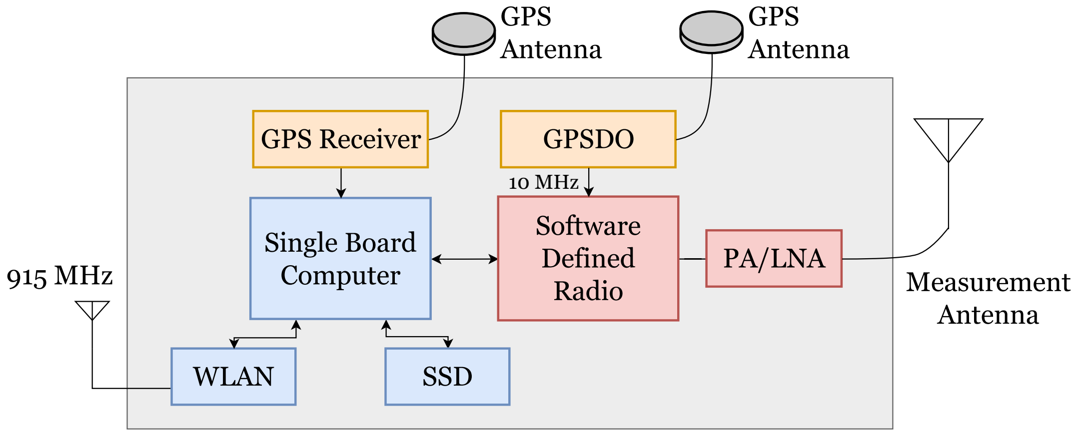

Figure 2.1 : A schematic of the measurement system.

The transmit power of the PA is 1 Watt across the sub-6 GHz band. On the receiver side, LNA provides a 20 dB gain with a 3 dB Noise Figure (NF). Effects of the both PA and LNA on the system are further discussed. There are several channel-sounding techniques such as pulse compression, correlation-based, and swept frequency. In this study, a correlation-based channel sounder is employed such that the drone platform needs to carry a low size, weight, and power (SWaP) payload which can only allow transmitting the maximum of 1 Watt RF signal.

Therefore, the receiver captures the sounding waveform and the correlation-based channel sounding provides higher processing gain in order to compensate for the low power limitation. The transmitted waveform includes a PN–sequence with the length 4095. Since a propagation channel is defined as a sum of discrete paths, the correlation function of an *m*–sequence is preferred since it provides higher resolution while distinguishing independent multi-path components [33]. The core of the channel sounder is an SDR. It delivers flexibility and stability at the same time. SDR architecture, as the naming implies, is mostly software defined, which is running on the host computer. The architecture of the transmitter and receiver are further explained in the following sections. The host computer, which is an SBC, runs the main software, which configures the SDR and captures the data generated by SDR. Also, experiment controls, GNSS positioning, and data storage are managed by the host computer.

The workflow of the sounding is shown in the Fig. 2.2. Preliminary information such as measurement frequency, measurement duration, and buffer length. With these parameters, it is possible to calculate the channel occurrence rate theoretically. The buffer length parameter is essential for the power integration. On the transmitter side, the SDR is configured through the SBC according to the measurement parameters such as carrier frequency and bandwidth. The SBC continuously generates waveform by reading a predefined PN sequence of length 4095 from the SSD, which is selected to support 1.6 Gbps data transmission need. The SDR performs all operations to convert IQ data to RF signals which are amplified up to 1 Watt before transmitting to the antenna.

On the receiver side, before starting the measurement recording, the SDR is configured through the SBC using the same parameters in the transmitter, including the carrier frequency and the bandwidth. During the experiments, the over–the–air signals are collected by the antenna, amplified by the LNA, and sent to the SDR, which performs all operations to convert the RF signals into the IQ data. The SBC is configured to hold the contiguous samples of IQ data and writes them periodically to the SSD to be further processed.

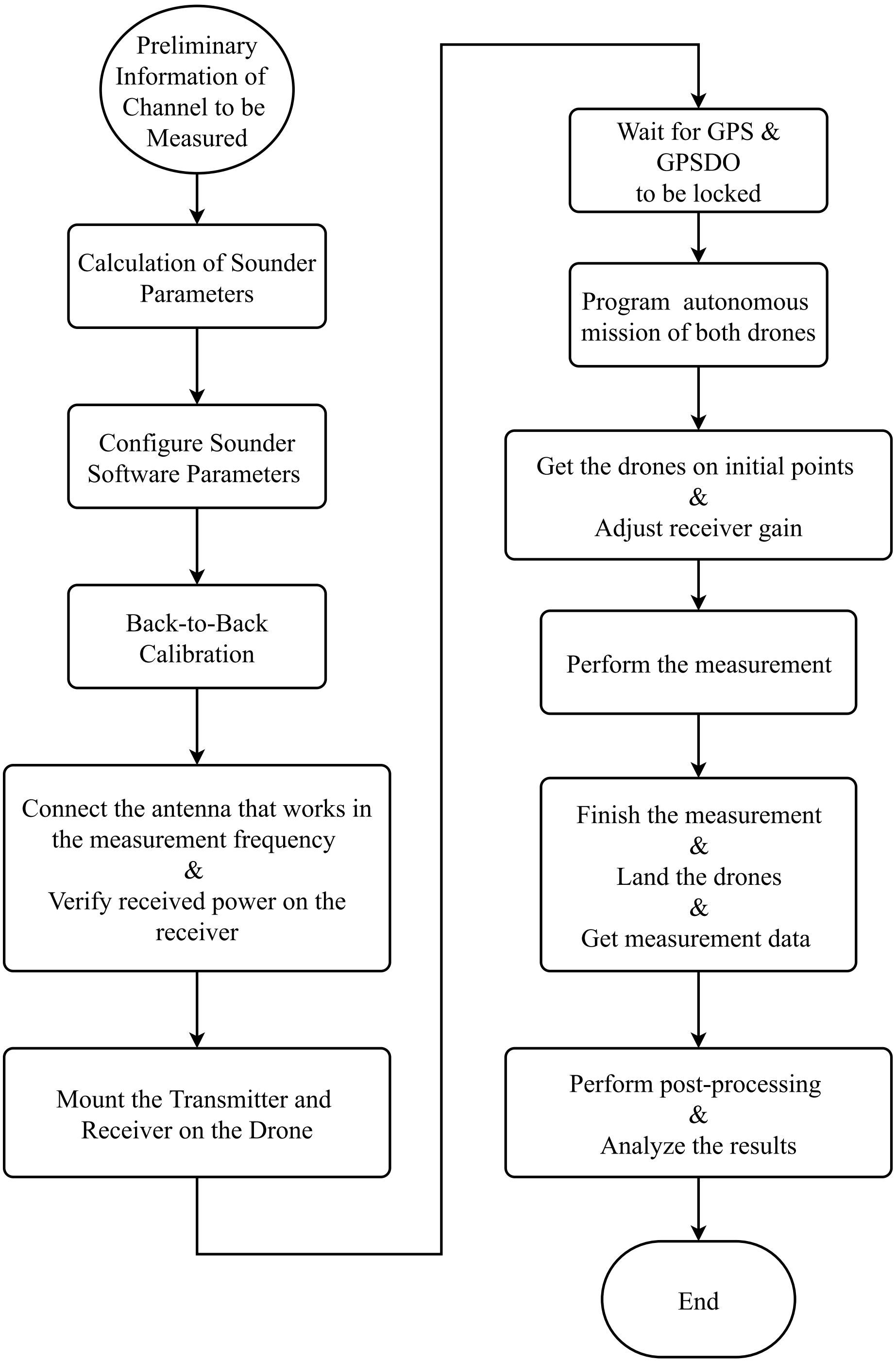

Figure 2.2 : Channel sounding workflow.

The sounder is designed to capture raw IQ samples of 50 MHz bandwidth up to 10 minutes long. However, depending on the measured channel, it became computationally burdensome data. The preliminary analysis of the needed capture data length and capture period is essential for this situation.

The GPSDO provides a 10 MHz clock which ensures precise frequency synchronization between the transmitting and receiving SDRs. The GPS receiver provides high-precision location measurements of both transmitting and receiving drones. The experiment measurements are recorded by adding the locations of measurement points so that the same scenario can be generated for the post-processing analysis. A WLAN interface operating at the carrier frequency of 915 MHz is used to manually and remotely control the channel sounder system.

2.2 Channel Sounder Sub-systems

In this section, the subsystems of the channel sounder are described.

2.2.1 Antennas

The antennas used for channel measurements are given in Fig. 2.3. The antennas must be lightweight, and their radiation pattern needs to be omnidirectional as much as possible. Because of the size weight and power (SWaP) restrictions of the drone payload, the antennas are chosen to be made by copper hardwire for specific measurement frequencies to meet SWaP and omnidirectionality requirements. On the other hand, there are minor deviations in the angular movement of the drones in the air. In order to compensate for this, the antenna pattern allows this slight movement to cause insignificant power changes. There are a pair of quarter-wave dipole antennae for each measurement frequency.

The radiation pattern of the antenna that is used for 2600 MHz Frequency band measurements is given in Fig. 2.4. The Azimuth and elevation slices of the pattern are shown in Fig. 2.5. The antenna has a gain of 1.75 dBi and a 3-dB beamwidth of 90°. Since the same topology is used for each antenna, the radiation patterns are similar.

The S_{11} parameter of the antenna is given in Fig. 2.6. For all antennas, the matching of the antenna is adjusted for empty bands closest to the operation bands. For instance, the

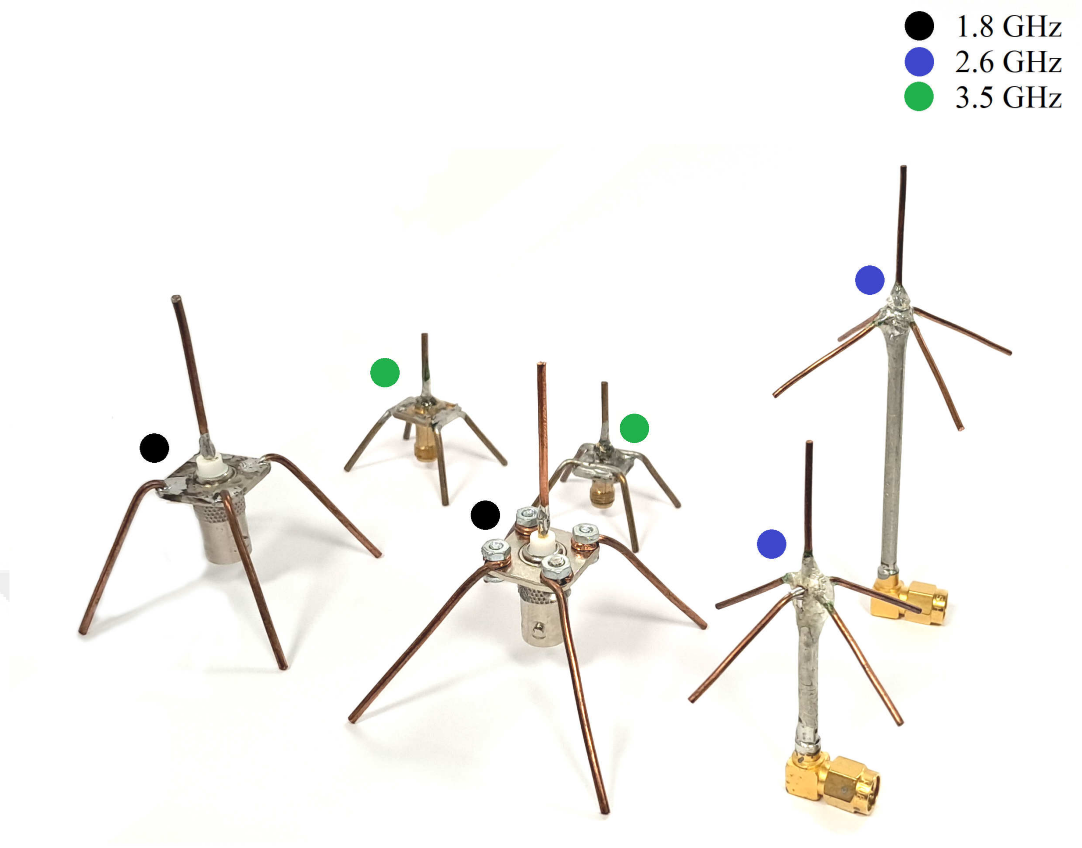

Figure 2.3 : Measurement antennas.

2600 MHz antenna is tuned to work best at 2560 MHz in order not to jam or interrupt service bands.

2.2.2 Software-Defined Radio

The SDR architecture brings flexibility to our channel sounder system. But this flexibility comes with costs such as low-quality RF frontend, low dynamic range, high throughput digital interface, and high-power processor for digital signal processing (DSP) operations. These costs need to be minimized by design decisions.

First of all, the low-quality RF frontend needs to be characterized by extensive measurements with the laboratory equipments. The analog transmit filters in the RFIC are widely tunable in 70 MHz up to 6 GHz center frequency and 200 kHz to 56 MHz bandwidth. [34]. The block diagram of the radio frequency integrated circuit (RFIC) is given in Fig. 2.7 [35].

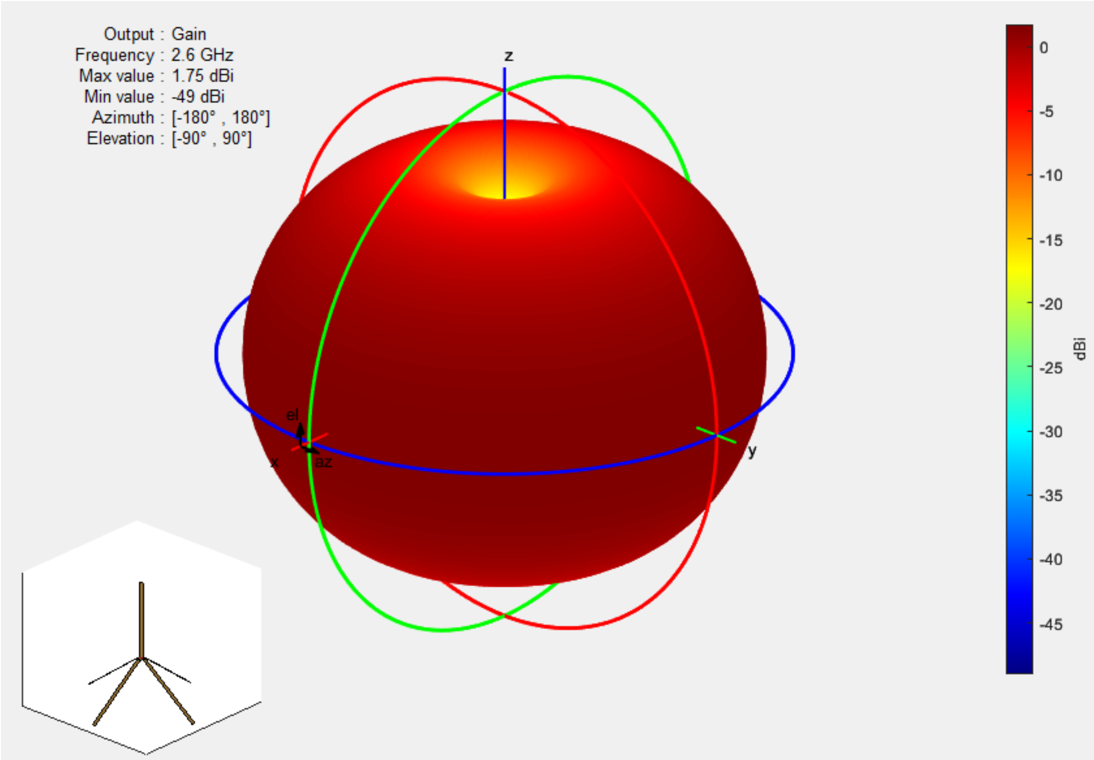

Figure 2.4 : Pattern of the antenna used in 2600 MHz-band measurements.

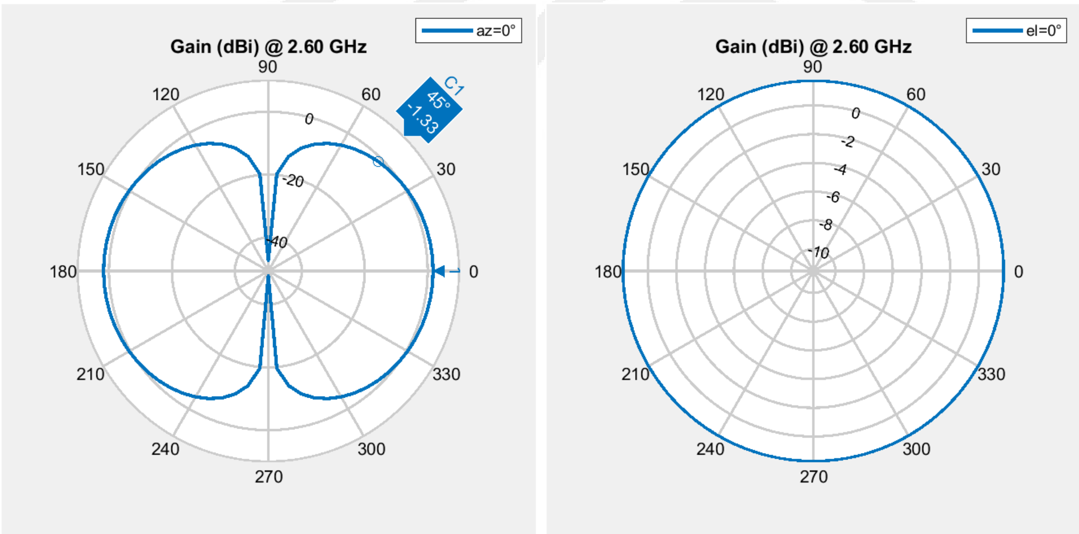

Figure 2.5 : 2600 MHz antenna - azimuth (left) and elevation (right) pattern.

While tuning into a frequency, the filters's responses are shown in Fig. 2.8. This results in the channel sounder's transmit side having bad adjacent channel isolation. On the other hand, it can transmit a wide bandwidth signal to increase the resolution of the measurements, which will be discussed in further sections. On the receiver side, this wideband filter becomes a problem because of nearby signal sources, such as

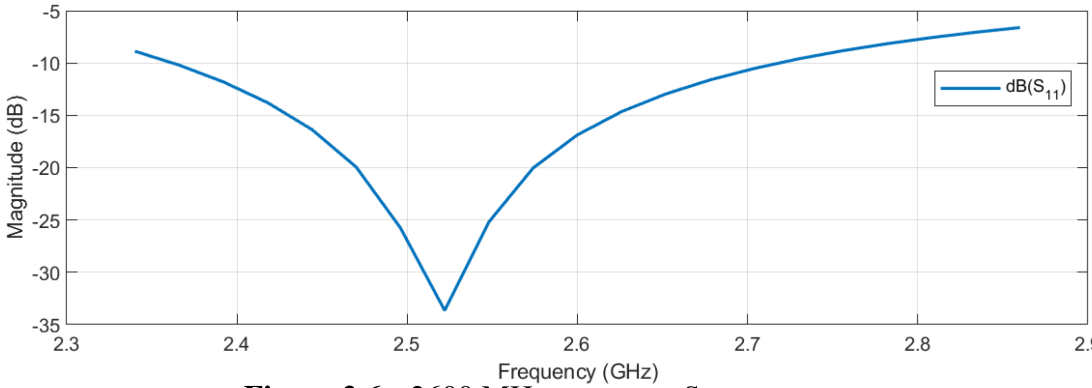

Figure 2.6 : 2600 MHz antenna - S_{11} parameter.

the sounder's control channel communication and the drone's telemetry signal. These signals interfere with the receiver and degrade measurements. So, it is essential to plan measurement frequency before the campaign. In addition, high-quality RF filters must be added in front of the receiver to diminish the interference effects.

Secondly, the SDR comes with 12-bit ADCs and 12-bit DACs where the receiver has a 72 dB dynamic range theoretically. In practice, the dynamic range is approximately 60 dB. The dynamic range parameter is significant for measuring power fluctuating channels. It is the limiting factor in measuring a channel without changing gain settings, which brings uncertainty into power measurements.

Thirdly, the SDR to host interface requires a high throughput connection to take contiguous buffers. If the receiving buffer overflows, the captured buffer contains two abrupt sequences. Also, if there is an underflow on the transmit buffer, the SDR fills up these voids with zeros. In both cases, the measurement at that point becomes useless. For this situation, the connection should be hardened by electrical or mechanical in order to avoid the effects. With some SDR devices, the throughput is limited to only 10-12 MSPS using a USB 2.0 interface.

To overcome the problems depicted previously, signal generation and signal capture processes are intended to be executed closer to the RFIC. Some of the SDR devices have system on chip (SoC), which contains both FPGA fabric programmable logic(PL) and low-performance ARM microprocessor processing system(PS). Generation and configuration of the transmitted signal require a host machine. With the help of the PS section of SoC, there is no need for a host device to be connected physically. The

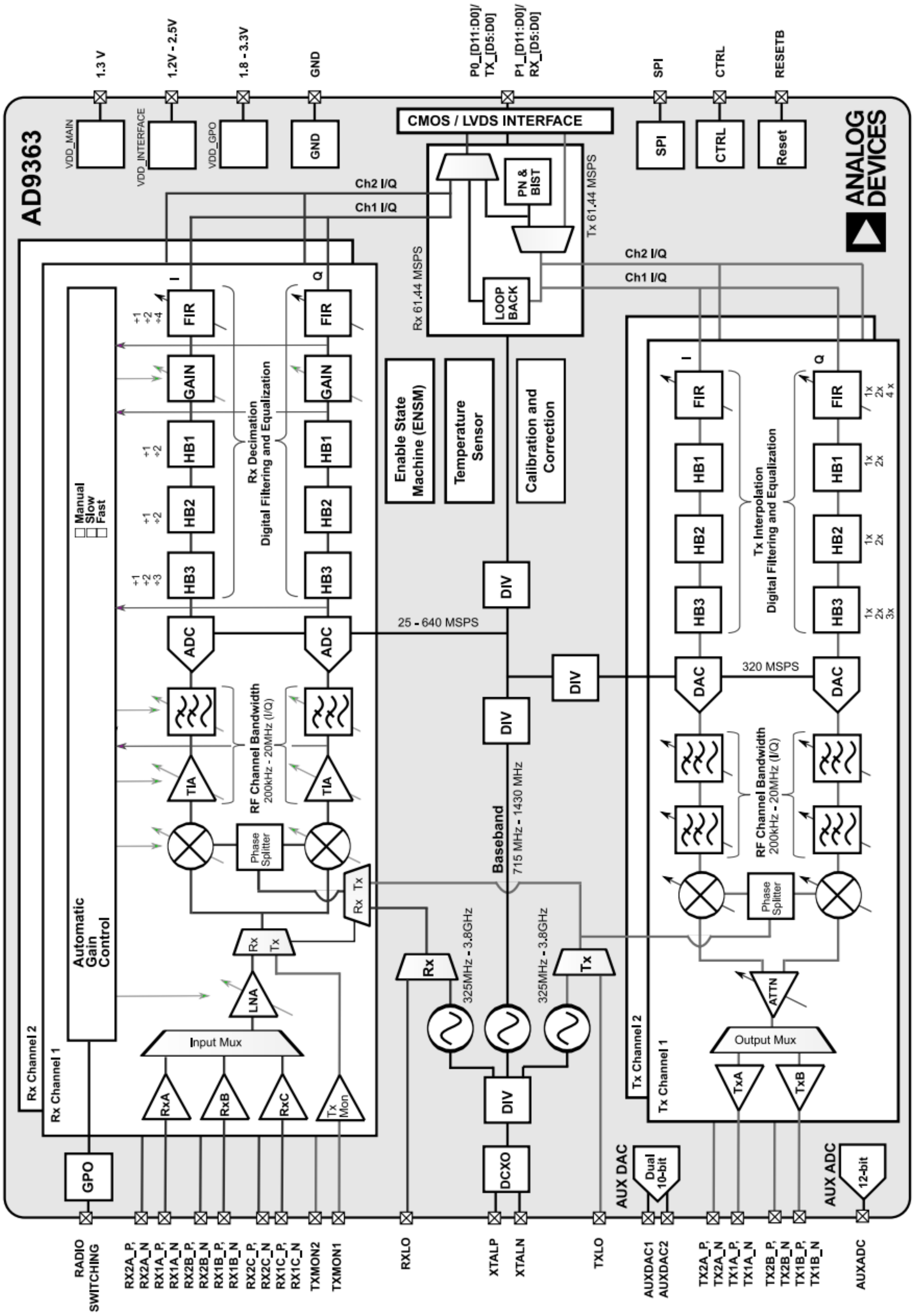

Figure 2.7 : Block diagram of the AD9363.

signal generation, RFIC configuration, and signal capture processes can be executed into the PS. Also, the PS has the same throughput as the PL section, which is connected

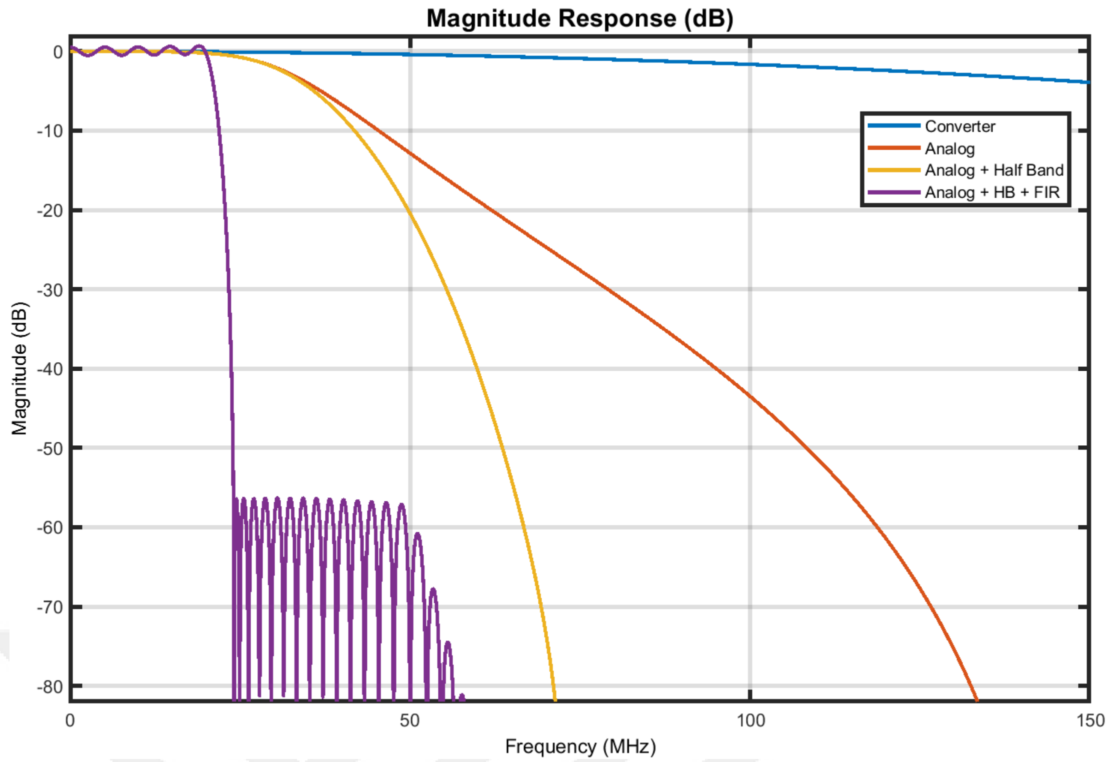

Figure 2.8 : Frequency responses of the filters in RFIC.

internally in the IC. This brings a great advantage over physical connections such as USB.

From the channel sounder perspective, the transmit processes are decided to be executed in the PS section. The SoC-based solution introduces great advantages, and the remaining bottleneck is the storage. For this reason, the channel sounder's receive tasks are decided to be executed into the host machine.

2.2.3 Mechanical

It is essential to have a reliable mechanical design for the installation of the Channel Sounder on the UAV. Designing mechanical components for air vehicles is a challenging task, taking into account factors such as temperature, mechanical strength, and vibration. These factors play a crucial role in the design process, particularly in UAV design. In addition, weight is a significant factor that needs to be considered. To address this, mechanical engineers at TÜBİTAK BİLGEM have designed a payload box specifically for the DJI Matrice 600 Pro UAV. The design prioritizes mechanical strength and lightness. The vibration problem is tried to be solved at every point during the placement inside the box. In particular, the USB 3.0 cable connection between the SDR and the SBC is very much affected by vibration due to its high data bandwidth, such that it is observed that this connection was disconnected in the middle of the measurement during the measurements. An Ethernet-based connection is chosen instead of USB, as the USB could cause problems again during flight.

Figure 2.9 : Payload carrying drone – DJI Matrice 600 Pro.

Photos of the channel sounder hardware are given in Fig. 2.10, 2.11 and 2.12.

Figure 2.10 : Channel measurement system – Enclosure and antenna ports.

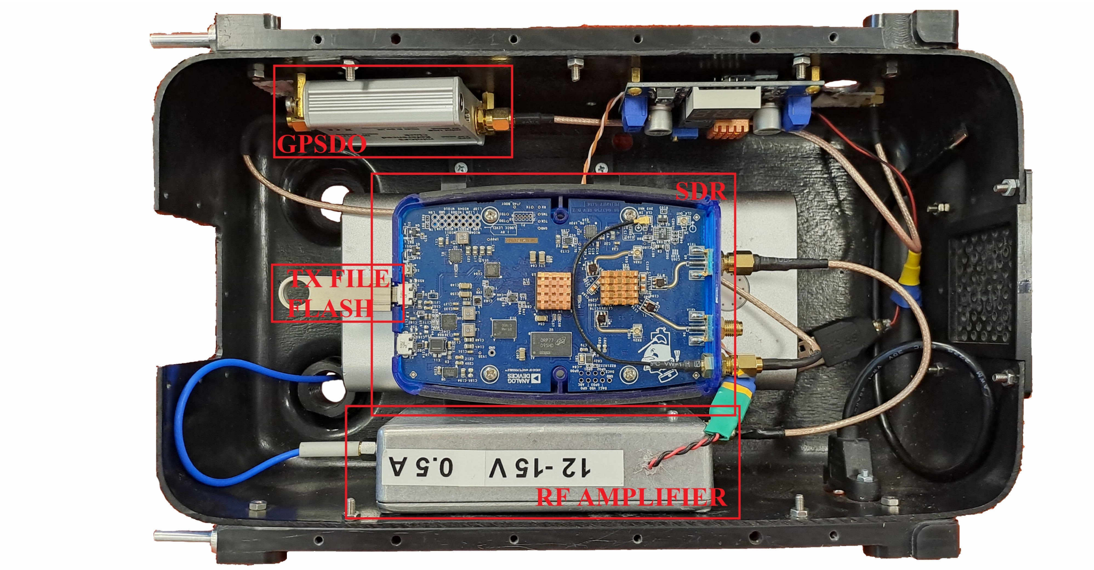

Figure 2.11 : Channel measurement transmitter – Inner placement of the subsystems.

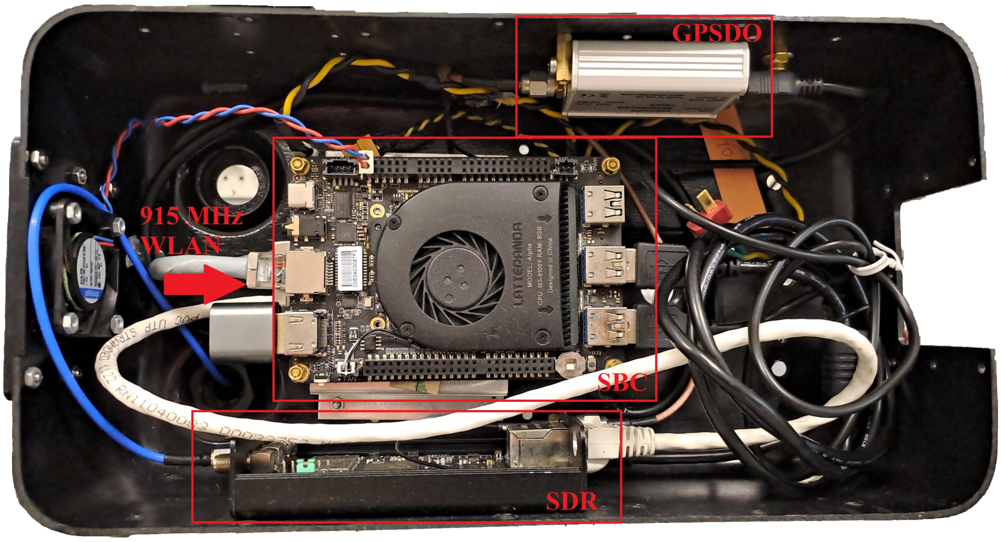

Figure 2.12 : Channel measurement receiver – Inner placement of the subsystems.

3. SIGNAL PROCESSING WORKFLOW

A priori knowledge of the channel to be measured plays an important role in optimizing design parameters. As mentioned earlier, collecting raw IQ data from the channel in a continuous manner poses a challenge for us in the later processing stages. Instead, we consider the theoretically computable channel coherence time parameter, which depends on the vehicle's speed and the measurement frequency. Since it is assumed that the channel does not change during this time, it is sufficient to take only one sample. For example, in the 3.5 GHz band, at a speed of 3 m/s, the channel coherence time is about 12 ms, which theoretically corresponds to about 82 different channels per second. With an unambiguous time resolution of 160 μs, a maximum of 6250 measurements can be made per second. It would be sufficient to take only 82 of these 6250 measurements, which corresponds to only 1.3% of the incoming IQ data. This reduction in the raw data amount makes the processing easier and more manageable.

As previously depicted, the channel sounder uses DSSS signal to measure the wireless channel by correlating with the known sequence. Next-generation storage solutions have become compact in terms of both storage space and bandwidth. A new generation M.2 SSD is integrated into the channel sounder. This made it possible to store 250GB of data in a device weighing only 8 grams. IQ buffers received in raw form from the SDR can be stored directly on the SSD and then fed to the desired signal processing algorithm. Therefore, the correlation, which is a lossy and irreversible process, is performed in the post-processing stage.

The post-processing analysis flow diagram is shown in Fig. 3.1. First of all, undesired recordings outside the measurement time interval are removed, and the measured IQ data are frequency-aligned in the signal pre-processing block. Furthermore, in the scenario and model parameter extraction block, the recorded location information is utilized to obtain the azimuth and elevation angles between TX-D and RX-D. Using the antenna pattern information together with the azimuth and elevation angles, the

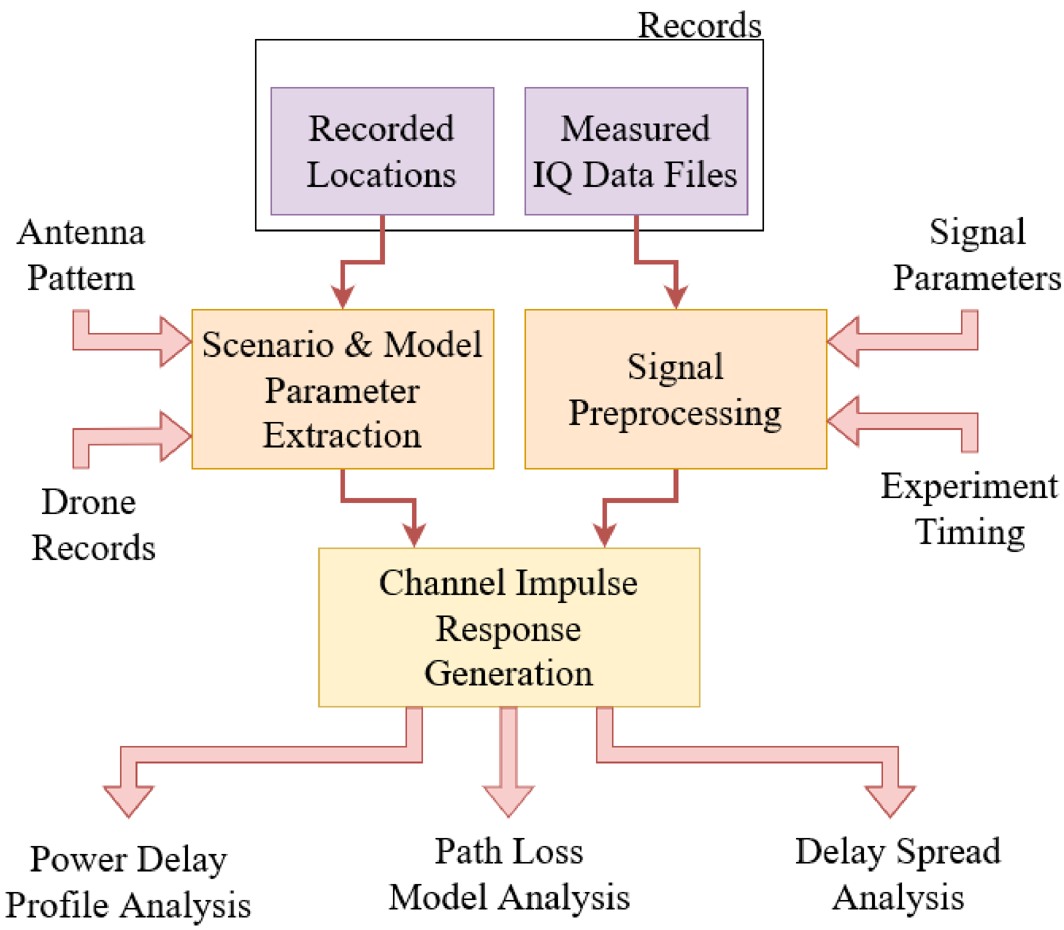

Figure 3.1 : Post-processing analysis flow diagram.

effects of the antenna patterns are normalized to the omnidirectional pattern. This normalization removes the effects of the antenna on the received signal so that only the channel effects are retained. Then, the losses due to the antenna patterns are calculated and sent to the CIR generation block which removes these losses on the received signal.

The CIR generation process is shown in Fig. 3.2. A coherent auto-correlation between the raw data and the known transmitted sequence is calculated to extract the CIR from the raw data.

The known transmitted sequence is repeated successively to increase the correlation gain. For example, the correlation gain is 36 dB, 42 dB, and 45 dB when the number of repeated known transmitted sequences is 1, 4, and 8, respectively. First, the intentionally added frequency offset is removed from the raw data and the FFT is applied. The repeated sequence is also passes FFT operation and its conjugate is multiplied by the other side. The resulting signal is then subjected to an inverse FFT

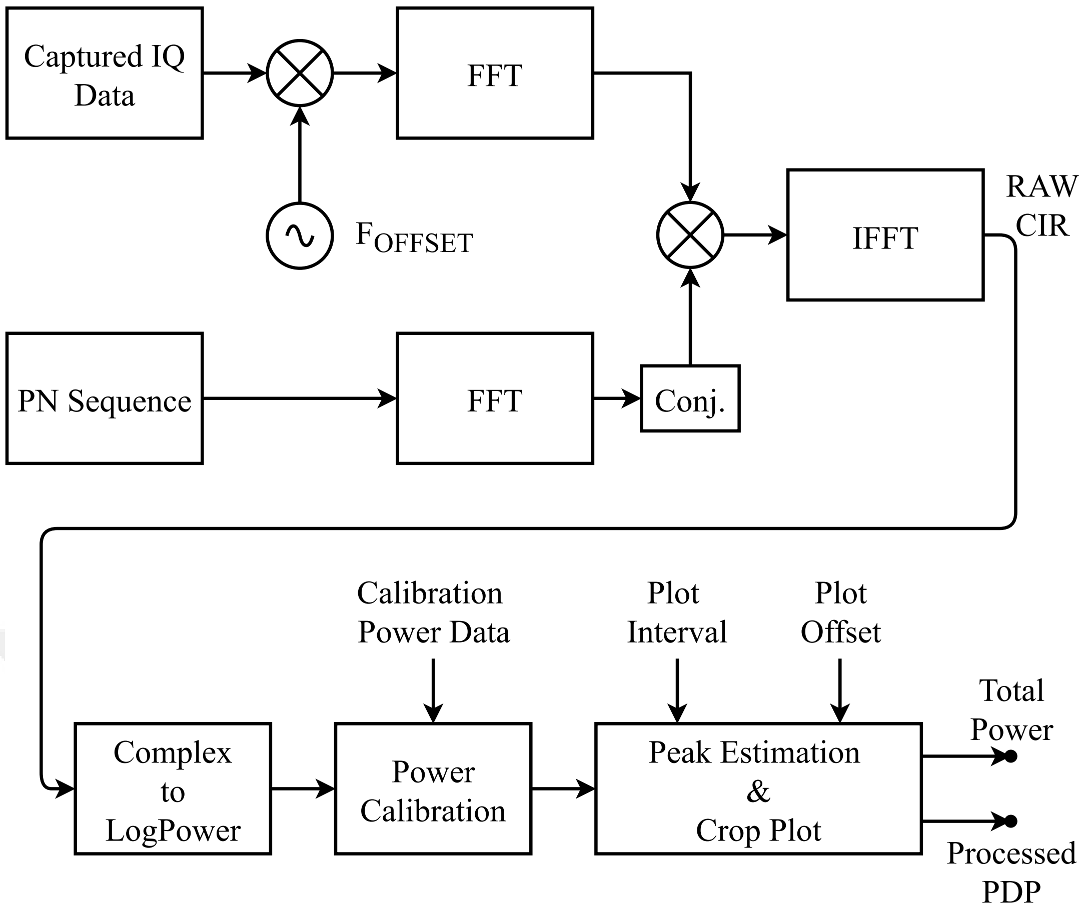

Figure 3.2 : Correlation process.

to obtain the raw CIR. The raw CIR data is then converted from complex IQ form to logarithmic power format as phase information is not used in the processing. At this point, it is calibrated with the power data previously obtained by the calibration process. Then, the part of interest is obtained by peak estimation on the CIR and the signals outside this part are neglected as they mostly contain noise. The duration of the part of interest is given externally as the plot duration and the time before the peak power point is given externally as the plot offset. The clipped PDP portion is used in subsequent processing. Also, the power peak is used for the next analysis.

Path Loss model analysis which is shown in Fig. 3.3, is based on the power values obtained during the entire measurement. The average path loss is obtained by fitting a 1D polynomial curve to the power values obtained for each distance. Note that the measured distances must be logarithmic. The path loss parameters are the results of this analysis. The path loss curve corresponding to these parameters is used in the subsequent analysis to normalize the measurement results.

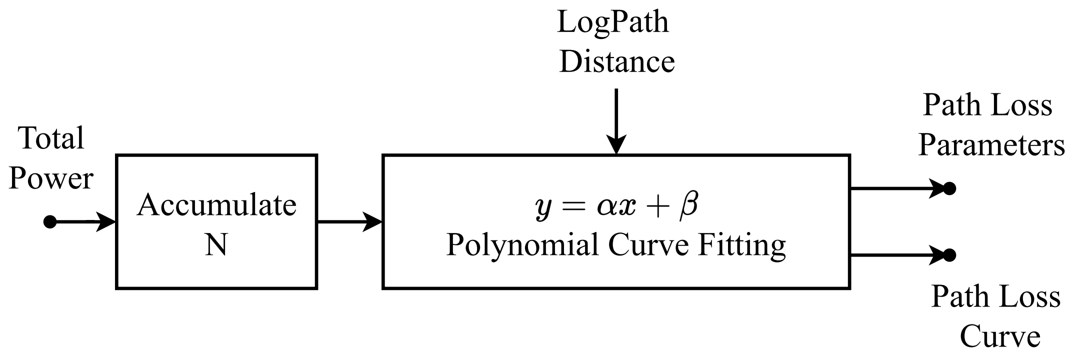

Figure 3.3 : Path loss model analysis process.

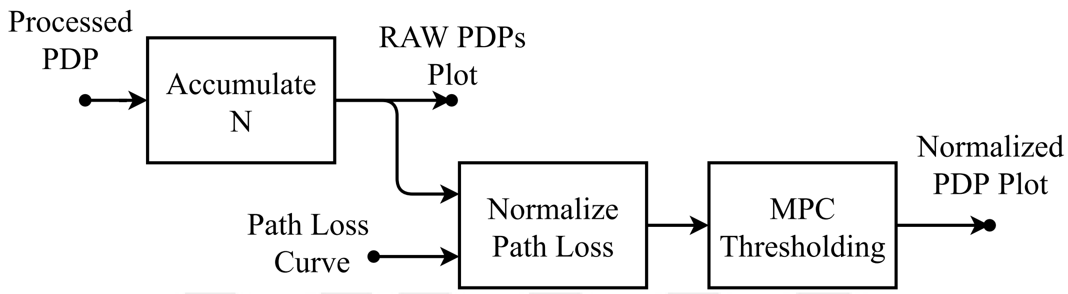

Figure 3.4 : PDP analysis process.

The PDP analysis process is shown in Fig. 3.4 where all measured PDPs are used for this analysis. In this way, multipaths in the measurement environment are clearly visible. First, the PDP at the corresponding distance is normalized using the values obtained from the path loss analysis. In this way, the strength of the multipath can be compared independently of the attenuation of the main signal. The CIR contains a direct-path component(DPC), multipath components (MPC), and noise components. The power threshold, which is used to decide whether an MPC is strong or weak, is set to 20 dB below the DPC power [36,37]. And the components that are below the power threshold are excluded from the CIR.

The RMS-DS analysis process is shown in Fig. 3.5. Normalized PDP are passed through the PDP mask which marks only the power samples so that the location of the received above-threshold signals with respect to time can be estimated. The RMS-DS value is calculated using these labeled samples. Once these values are calculated for the whole measurement, the RMS-DS statistics can be extracted by statistical analysis. In addition, the values from the PDP mask are masked again as either LOS or non–line–of–sight (NLOS) samples. As a result of this process, the powers of the

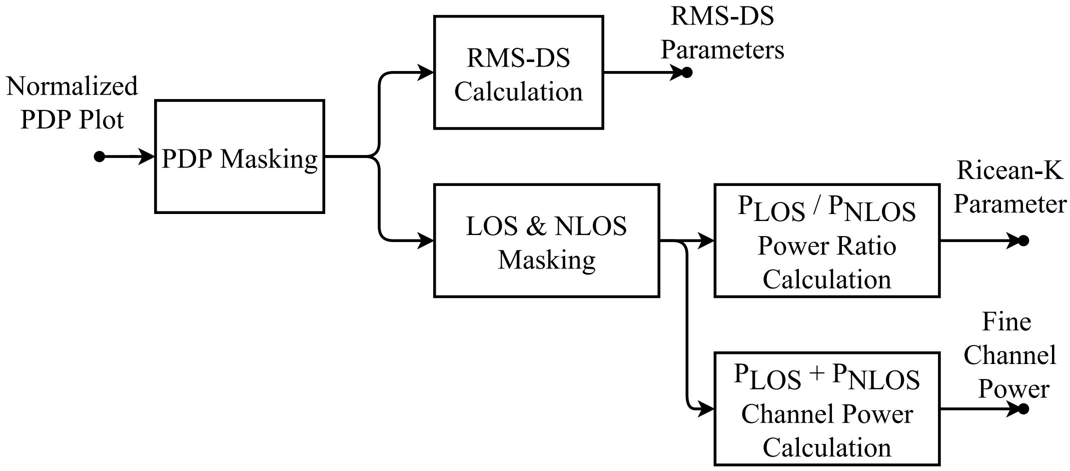

Figure 3.5 : RMS-DS analysis process.

received LOS and NLOS components are calculated separately. While the Ricean-K parameter can be calculated from the ratios of these two powers, the precise channel power can be calculated from their sum.

3.1 Calibration of Channel Sounder

Back-to-back calibration is essential to the verification of the channel sounder. A stationary channel realized in the laboratory with cables and attenuators is connected between the transmitter and the receiver. The measurements from this channel serve as a basis for other field measurements and analysis of the channel sounder. As an example, the calibration at 3500 MHz is provided. Fig. 3.6 shows the connections between the channel sounder and the generated channel. The transmitter output power is measured using a Rohde & Schwarz FSW43 model Spectrum Analyzer. It is observed that the transmitter had an RF output power of 27.3 dBm for 3500 MHz. A channel that consists of cable and attenuators, a 15.24 meter-long test cable, one 3 dB attenuator, and two 30 dB attenuators is measured. Based on the loss values shared on the datasheet and the power measured on the spectrum analyzer, the total loss should be 74.6 dB. In this case, -47.3 dBm power is expected at the receiver side. This value is equated to the correlation output value at the receiver to obtain the power calibration value. The raw data from the Channel Sounder Receiver at the correlator output is shown in Fig. 3.7. The correlation peak value is at 78.4 dB. To equalize this value to

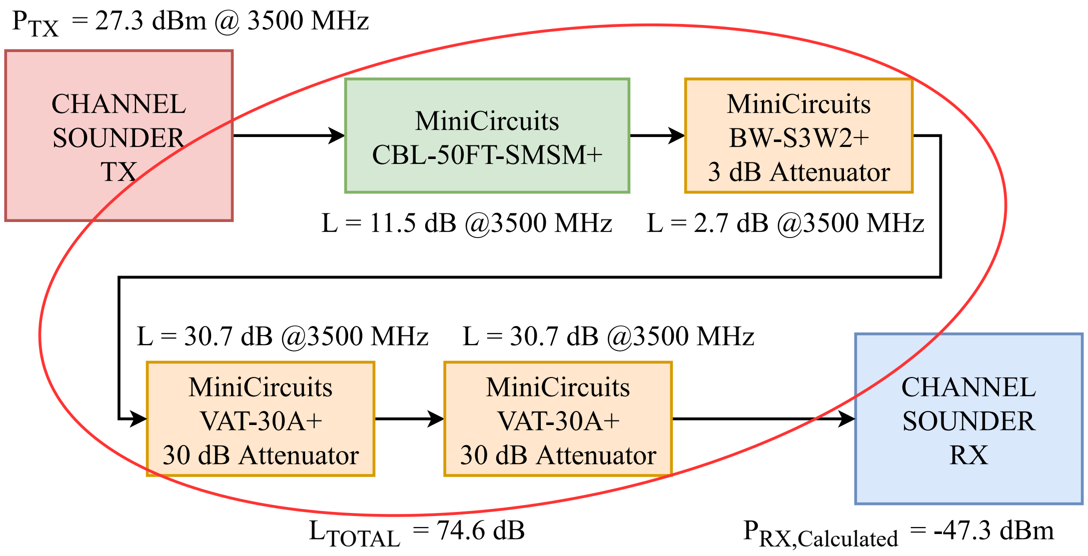

Figure 3.6 : Back-to-back calibration – connection diagram.

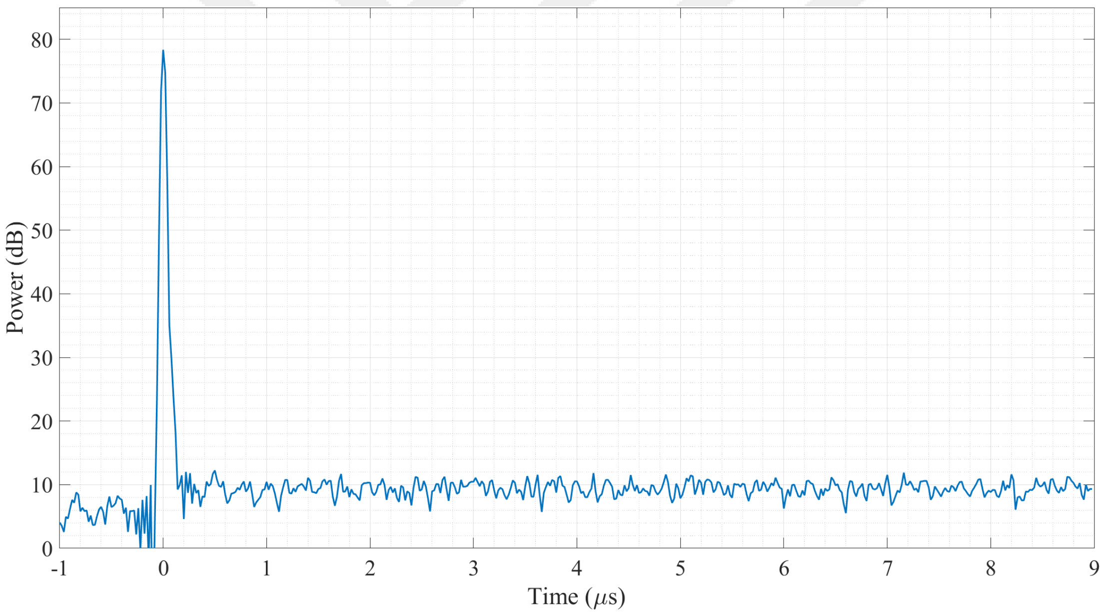

Figure 3.7 : Calibration measurement correlator output.

-47.3 dBm, 125.7 dB is subtracted from the power values obtained at the correlation output. This value is utilized as the power calibration value for the measurements at 3500 MHz.

The PDP analysis with all the received calibration data is shown in Fig. 3.8. The peak value of the incoming signal is distinguished by at least 60 dB from all white

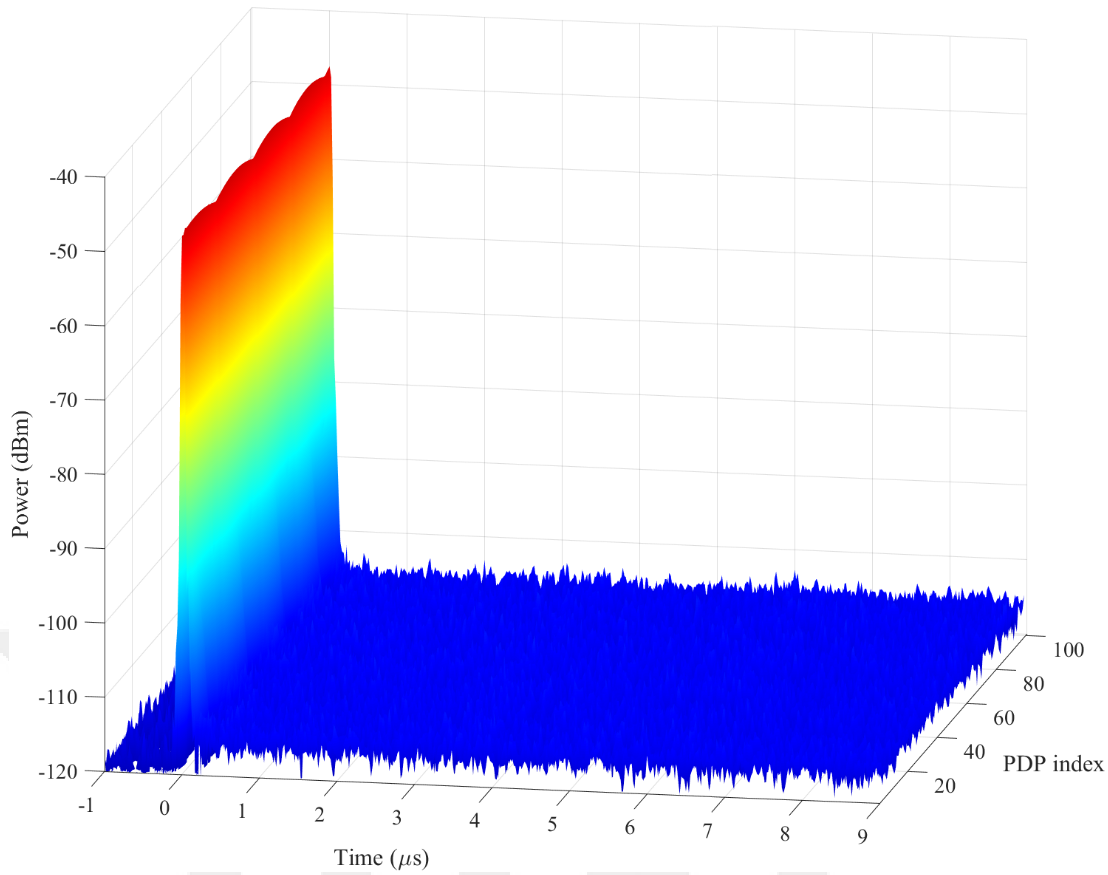

Figure 3.8 : Calibration measurement PDP analysis output.

noise and in-device distortions. The receiver noise floor is -115 dBm. The reason for the fluctuation in the peak of the signal is that the test is performed in a laboratory environment without GNSS signals. In this case, the transmitter and receiver are not perfectly frequency synchronized. As a result, the sample rate offset (SRO) between the transmitter and the receiver causes this effect.

RMS-DS analysis was performed on the calibration measurement and the results are shown in Fig. 3.9. Except for small errors due to the SRO, the RMS-DS values have a mean of 12.65 ns and a standard deviation of 0.11 ns. This means that the channel sounder system can measure with high precision. The average RMS-DS value is subtracted from the other measurements taken as calibration data for this analysis.

As mentioned earlier in the power measurements, both coarse and fine power measurements are available. In these measurements, the value of the received correlation peak is taken as the coarse power measurement. Since this value is a single

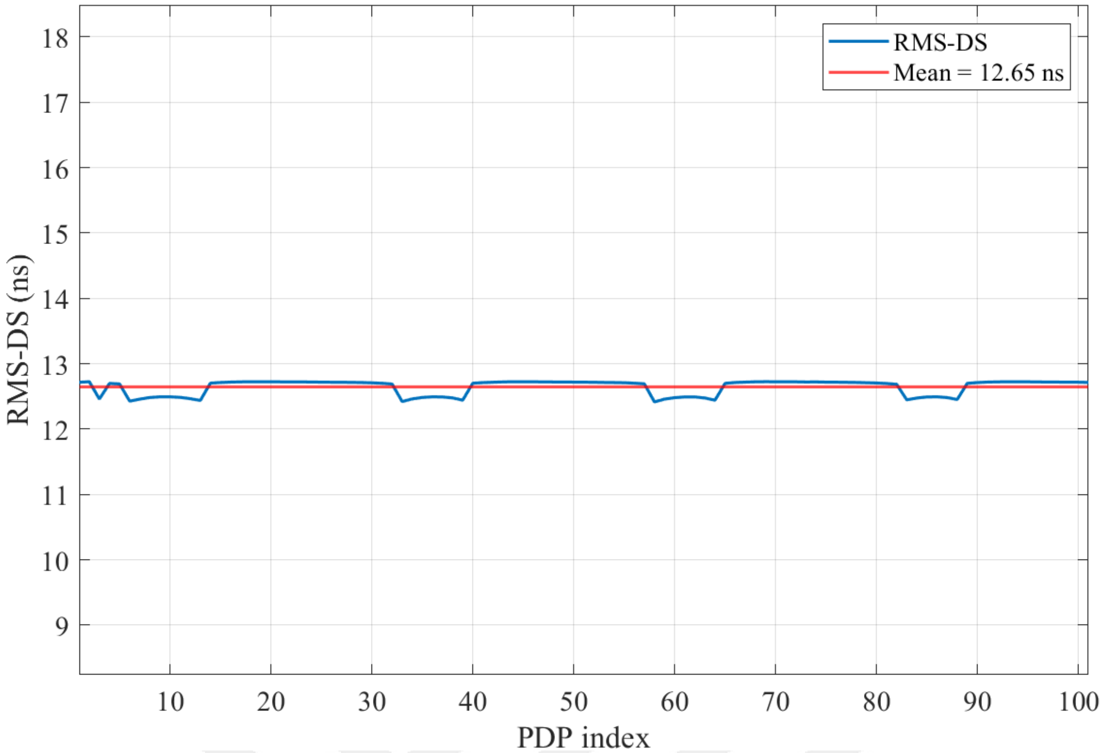

Figure 3.9 : Calibration measurement RMS-DS analysis output.

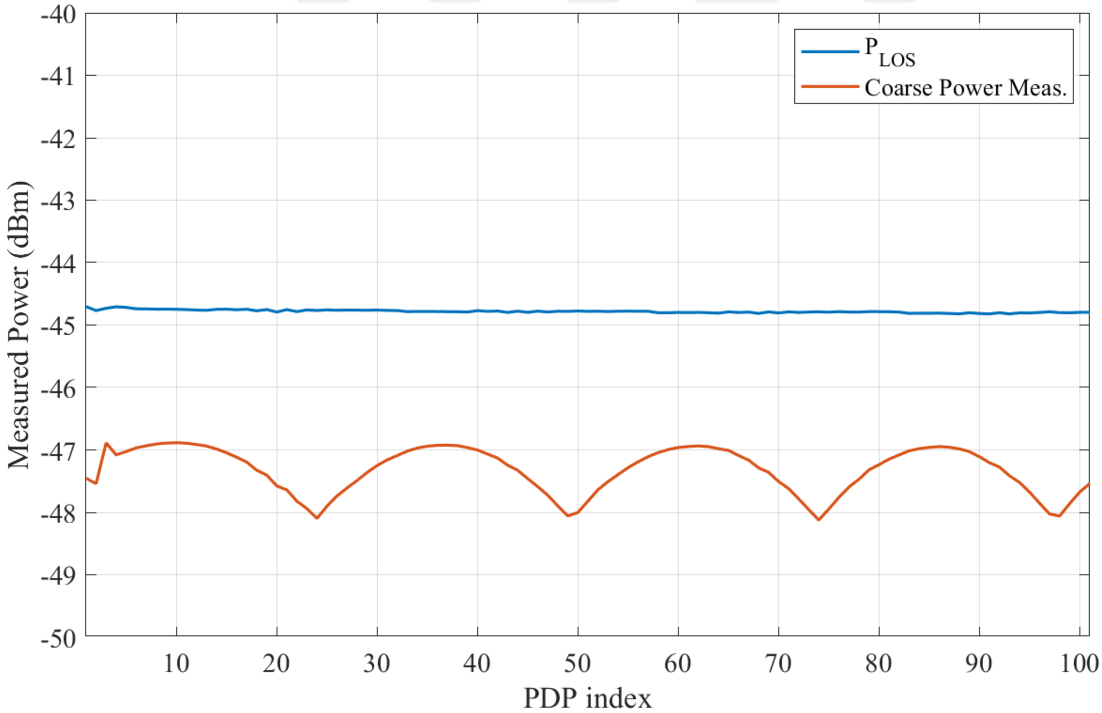

Figure 3.10 : Calibration measurement power measurement output.

sample, it does not include the power of the entire peak. This value may fluctuate due to effects such as SRO. As can be seen in the red curve in Fig. 3.11, the power value is oscillated by 1 dB during the measurement.

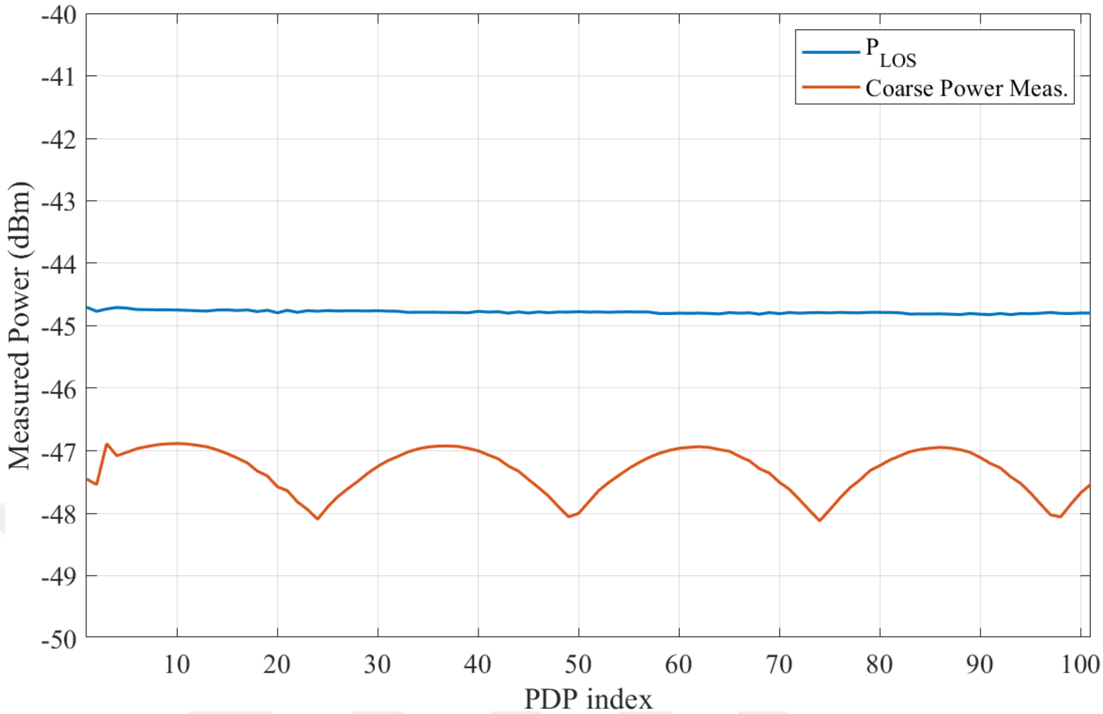

Figure 3.11 : Calibration measurement power measurement output.

The fine power measurement is calculated to include all signals from the peak, not the power of the incoming peak. The results of this measurement are shown in the blue curve in Fig. 3.11. Since it includes the power of all samples, it remains unchanged throughout the measurement and is about 3 dB higher than the coarse power. This value was used when analyzing the data from the field measurements.

As a result, it is demonstrated how the implemented channel measurement system behaves under ideal conditions. This section describes the calibration of an SDR-based system at a single frequency. It is observed that for outdoor wireless channels, the system has sufficient resolution considering all the interference effects present in the system, and most importantly, the measurement results do not change significantly over time. Before the measurements, this calibration step must be performed for the frequency band to be measured.

4. EXPERIMENTS AND RESULTS

4.1 Measurement Environment

The measurements were carried out at the TUBITAK Gebze campus as shown in Fig. 4.1 using two DJI Matrice 600 Pro drones. The campus terrain is mostly hilly and forested. The buildings on the campus are concentrated in a single area, but there are also sparse groups of buildings in the forested part. In this sense, the measured environment resembles rural settlements. The necessary approval to fly the drone and conduct the experiment was obtained from the campus administration. Measurements of A2A, receiver drone (RX-D) It is performed with M_1 at the measurement site and transmitter drone (TX-D) initially at the measurement site M_2 as shown in Fig. 4.1. Both UAVs have a height of 100 meters, and the initial distance between them is 85 meters. Measurements are taken every 100 ms with RX-D stationary, while TX-D flies autonomously from M_2 to M_3 in Fig. 4.1 along a 1 km straight trajectory at a constant speed of 3 m/s at the same altitude. In A2G measurements, RX-D is at the measurement point M_4, and the TX-D flies from M_2 to M_3 along a straight trajectory of 1 km at a constant speed of 3 m/s at the same altitude.

Figure 4.1 : Measurement site and flight route.

This choice of measurement scenario was chosen to compare the A2A and A2G channels. The measurement altitude was chosen below the legal limit of 120 meters in order to avoid problems with air traffic during the measurement.

The measurement scene is shown in Fig. 4.2. The measurements of A2G were

Figure 4.2 : A2G measurement scene.

performed with the receiving antenna placed on an extended mast at point M_4 with the receiving antenna 3 meters above the ground. The 1-kilometre measurement distance followed by TX-D takes approximately 6 minutes at a speed of 3 m/s. Note that this time is based on the limited flight time of the drones due to battery limitations.

The measurement procedure is explained as follows. Initially, TX-D starts to broadcast the sounding waveform. After that, RX-D and TX-D autonomously fly from the takeoff area shown in Fig. 4.3 to the measurement points M_1 and M_2, respectively.

Figure 4.3 : The RX-D and the TX-D at the takeoff points.

The drones take off in sequence to avoid possible collisions during autonomous take-off. It is shown in Fig. 4.4 and Fig. 4.5.

When the RX-D arrives at M_1, the TX-D begins to takeoff and goes to M_2. Then we remotely send a start command to RX-D which begins recording the measurements while TX-D flies through the flight route from M_2 to M_3. We remotely send a finish command to RX-D which stops recording the measurements when TX-D arrives M_3,

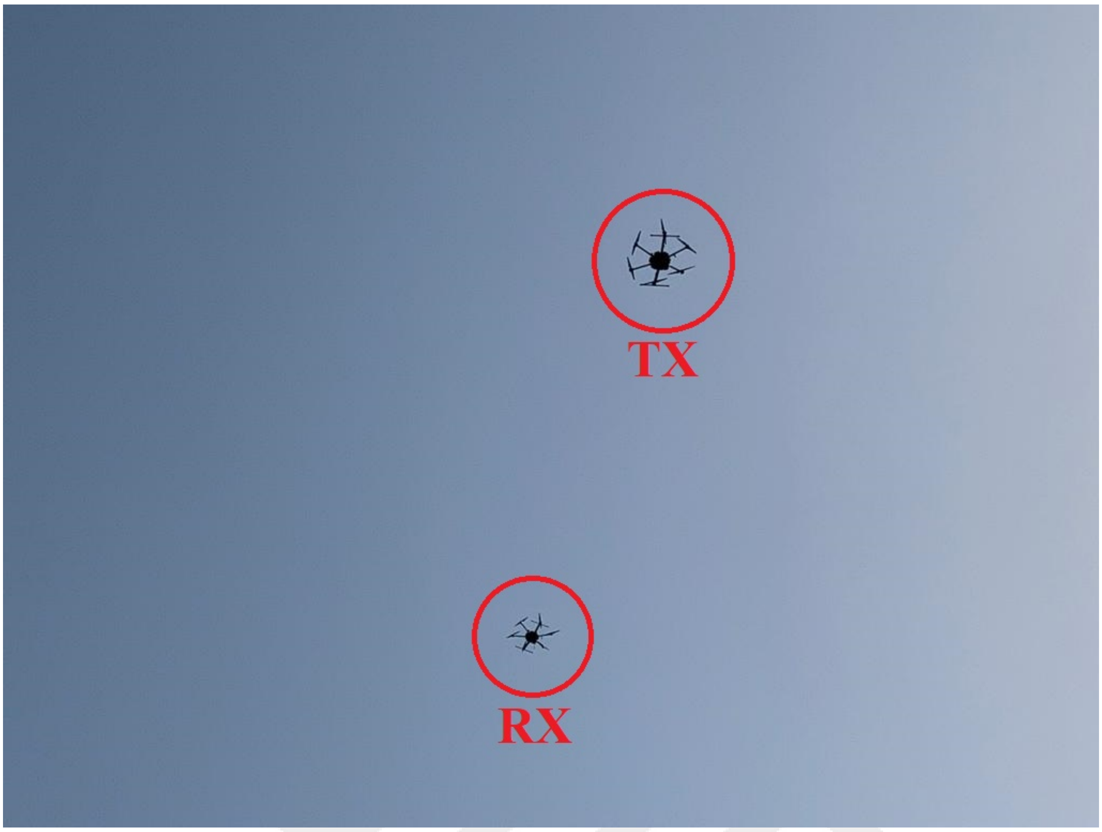

Figure 4.4 : The RX-D and the TX-D on the air.

and then both drones come back and land. During the experiments, the flight logs of the drones and the IQ records are continuously saved to be used for offline post-processing.

The channel sounder parameters used in the measurements are given in Table 4.1. The measurements were taken at 1.75, 2.56, and 3.5 GHz bands. The waveform parameters are constant in these bands. The only parameter that changes between the measurements is the output power of the transmitter, which varies depending on the frequency.

The channel measurement configuration is strongly dependent on the polarisation. The effects or surface properties of the reflectors in the measured channel change according to the polarization. The practical use cases tend to employ both polarizations according to the target application. The measurement configurations for A2G cases are taken as vertical polarization as shown in Fig. 4.6. On the other hand, horizontal polarization is preferred for A2A configuration as shown in Fig. 4.7.

Figure 4.5 : Measurement site while taking measurements.

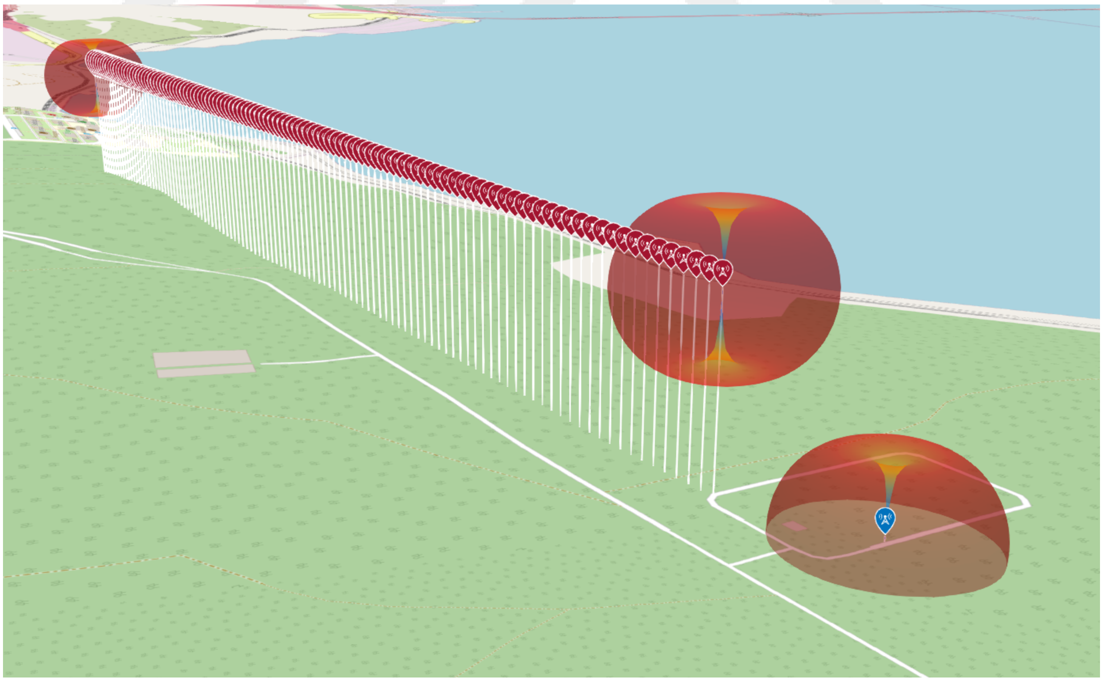

Figure 4.6 : A2G antenna patterns on measurement site.

Table 4.1 : Channel Sounder parameters.

Parameter	Exp. 1	Exp. 2	Exp. 3	Exp. 4
Configuration	A2G	A2G	A2G	A2A
Polarization	V	V	V	H
Center Frequency	1.75 GHz	2.56 GHz	3.5 GHz	3.5 GHz
Bandwidth	50 MHz	50 MHz	50 MHz	50 MHz
PN Sequence Length	4095	4095	4095	4095
Delay Time Resolution	20 ns	20 ns	20 ns	20 ns
Maximum Delay Time	160 μs	160 μs	160 μs	160 μs
Transmitted Power	28.2 dBm	28.1 dBm	27.3 dBm	27.3 dBm

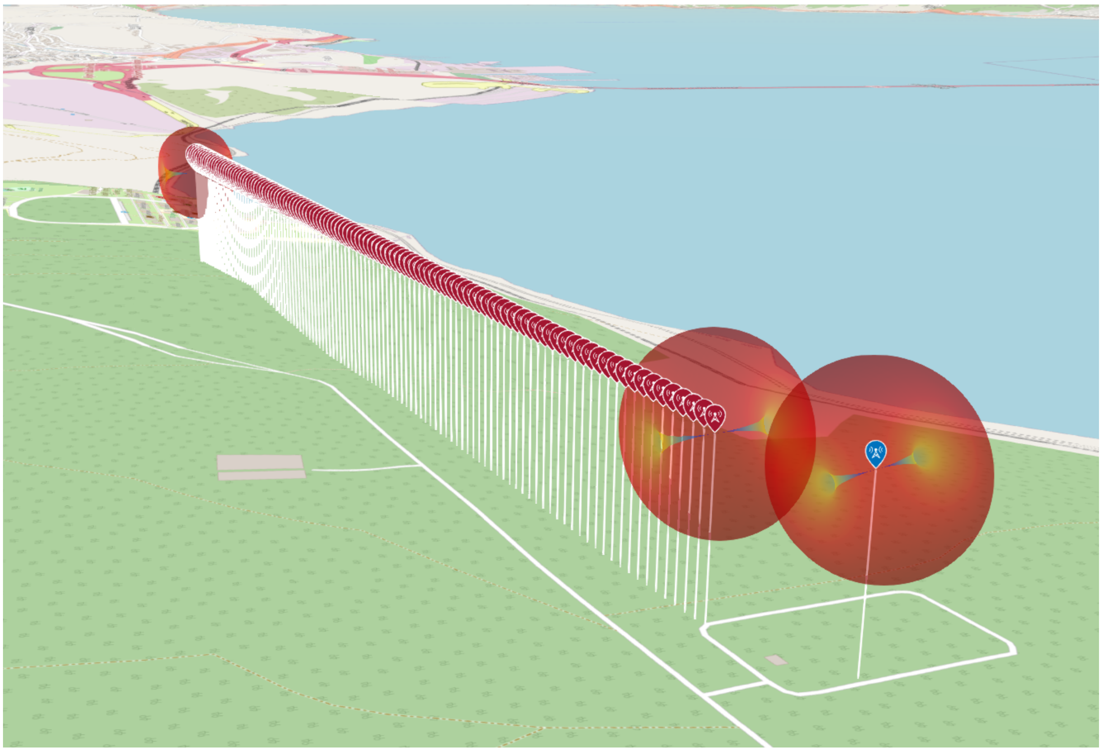

Figure 4.7 : A2A antenna patterns on measurement site.

4.2 Measurement Results & Discussions

In this section, analyses of the measurement results are presented for the field measurement scenarios. After generation of the CIR, which is explained in Chapter 3, it is utilized to obtain important channel characteristics such as PL model, PDP, RMS-DS, and Ricean K-factor. In this section, the measurement results of these characteristics are presented for experiment scenarios. The summary of the measurement results is given in Table 4.2.

Table 4.2 : Analysis results.

		1750 A2G	2560 A2G	3500 A2G	3500 A2A
η		2.0608	1.9832	1.987	2.0415
PL_0 (dB)		33.2	37.65	42.65	41.88
σ_τ (ns)	Mean	30.16	23.74	39.4	36.9
	STD	25.74	22.43	35.8	24.5
	Max	214.38	190.26	278.1	147.96
	Min	0.27	0.7584	2.16	0.0523
Ricean-*K* Factor (dB)	Mean	18.87	20.0	18.2	24.3
	STD	2.83	2.52	2.55	14.89
	Max	28.42	29.8	27.9	75.1
	Min	10.10	13.2	10.88	11.55

4.2.1 Path Loss models

Fig. 4.8, 4.9, 4.10 and, 4.11 show the path loss results of the measurement, along with the results of the FSPL and the FE2R models for the scenarios.

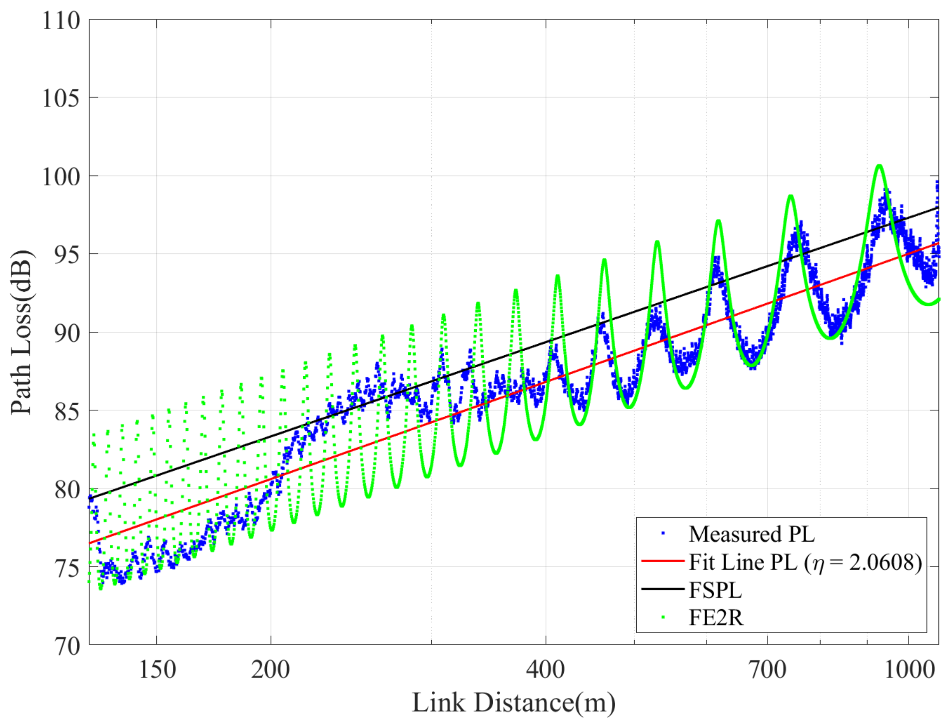

Figure 4.8 : 1750 MHz-band Path loss models for A2G.

The log-distance PL model parameters are given in Table 4.2. The path loss exponent values are 2.0608, 1.9832, 1.987, and 2.0415 for 1750 MHz A2G, 2560 MHz, and 3500 MHz A2G & A2A scenarios, respectively. These values are close to the FSPL

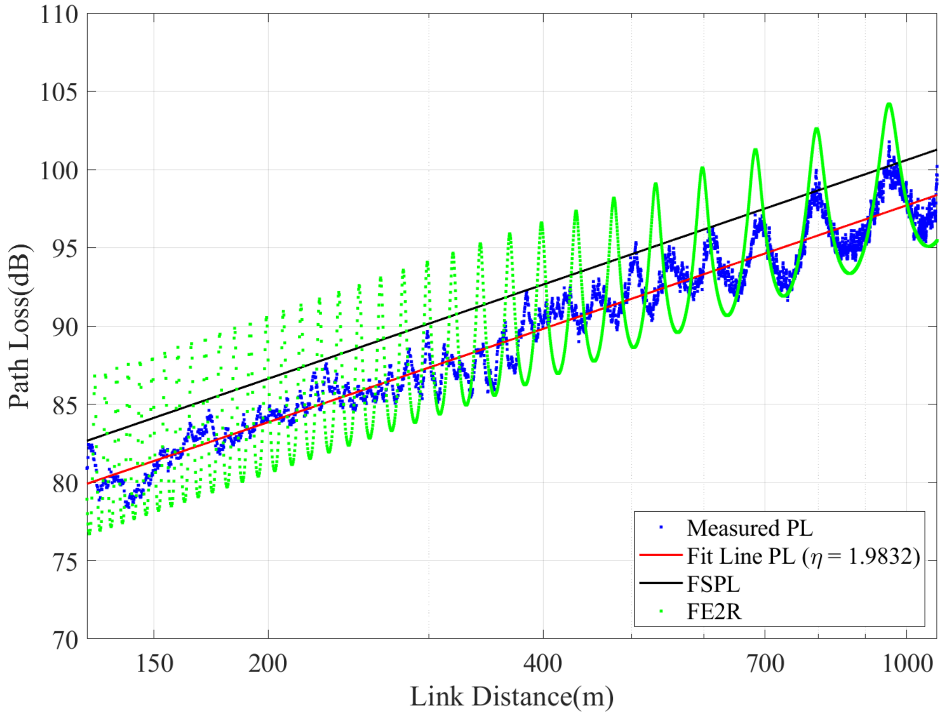

Figure 4.9 : 2560 MHz-band Path loss models for A2G.

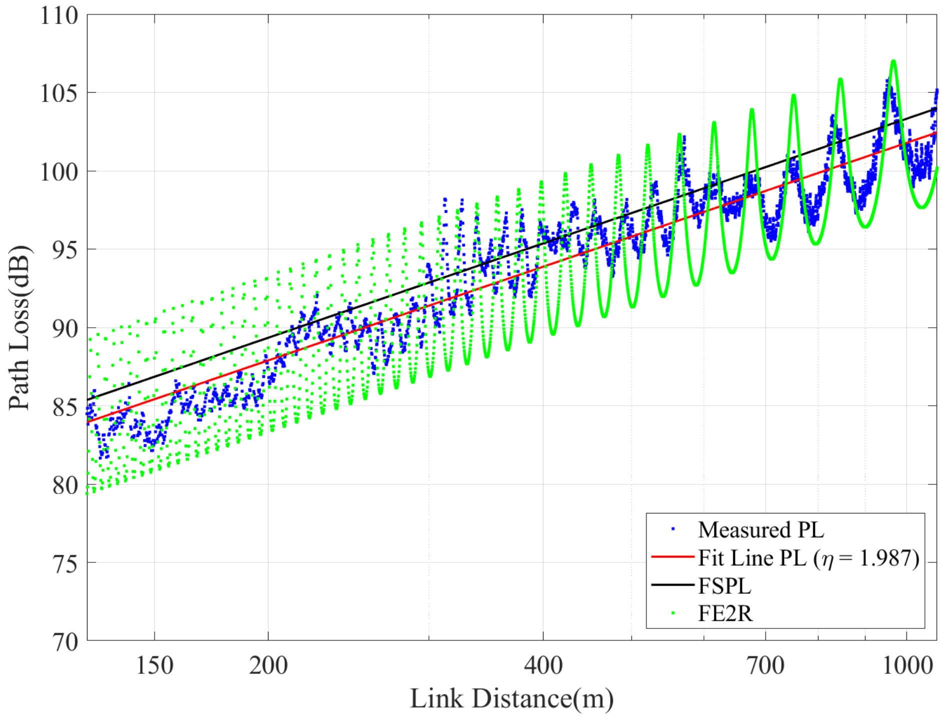

Figure 4.10 : 3500 MHz-band Path loss models for A2G.

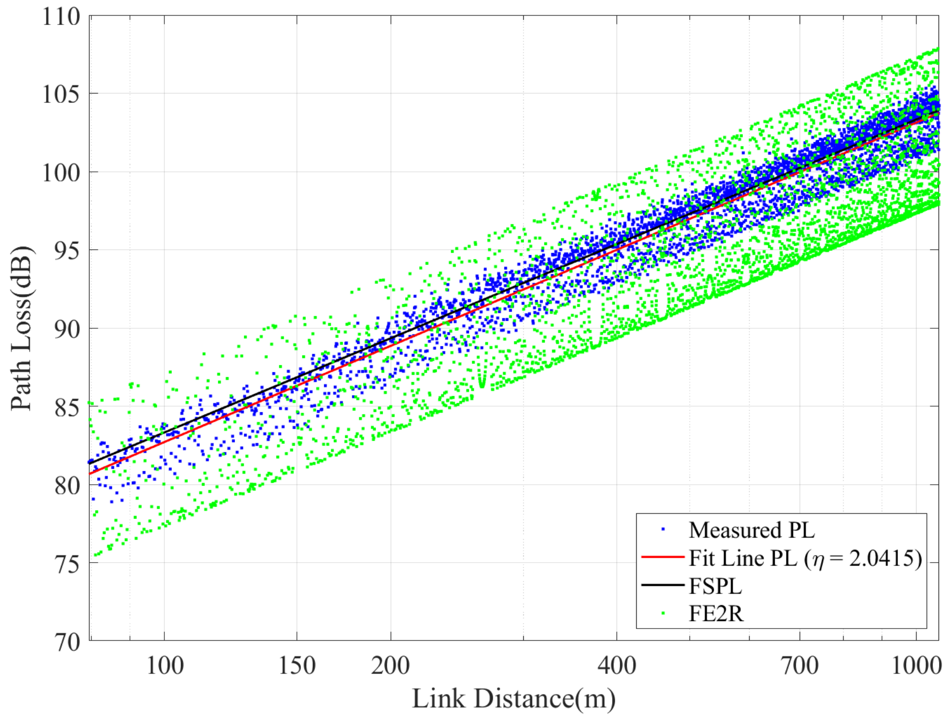

Figure 4.11 : 3500 MHz-band Path loss models for A2A.

path loss, as expected. The most noticeable feature in the measured PL results of the A2G scenarios is the two-way-induced lobes. The width and depth of these lobes are different at each frequency. It is much more significant at 1750 MHz compared to other frequencies. As the frequency increases, the depth of these lobes gradually decreases. This is because when the multipath component reaches the receiver in the opposite phase to the main path component, it causes the highest path loss by canceling it. If the frequency is higher, the reflected component from the ground will suffer more path loss and will have less effect. On the other hand, as the frequency increases, this fluctuation in power becomes more frequent. Therefore, it can be deduced that for UAV communication applications, where diversity techniques such as MIMO are not used, the probability of the long-term signal outage decreases with an increase in frequency. In the A2A measurement results, the PL follows a straight trend as expected, but the measured PL values are scattered within a constant envelope of 5 dB. Adding the measurement parameters to the FE2R model, it is possible to say that the model result scatters in accordance with the measurements.

4.2.2 Power delay profile

The results of unprocessed PDP measurements are presented in Figs. 4.12, 4.14, 4.16 and 4.18, where the direct path and reflections are scattered and vary with time in the A2G scenarios. On the other hand, Figs. 4.13, 4.15, 4.17 and 4.19 present the log-distance PL normalized and thresholded PDP measurements. The PL-normalized results are used to conduct RMS-DS and Ricean K-factor analyses.

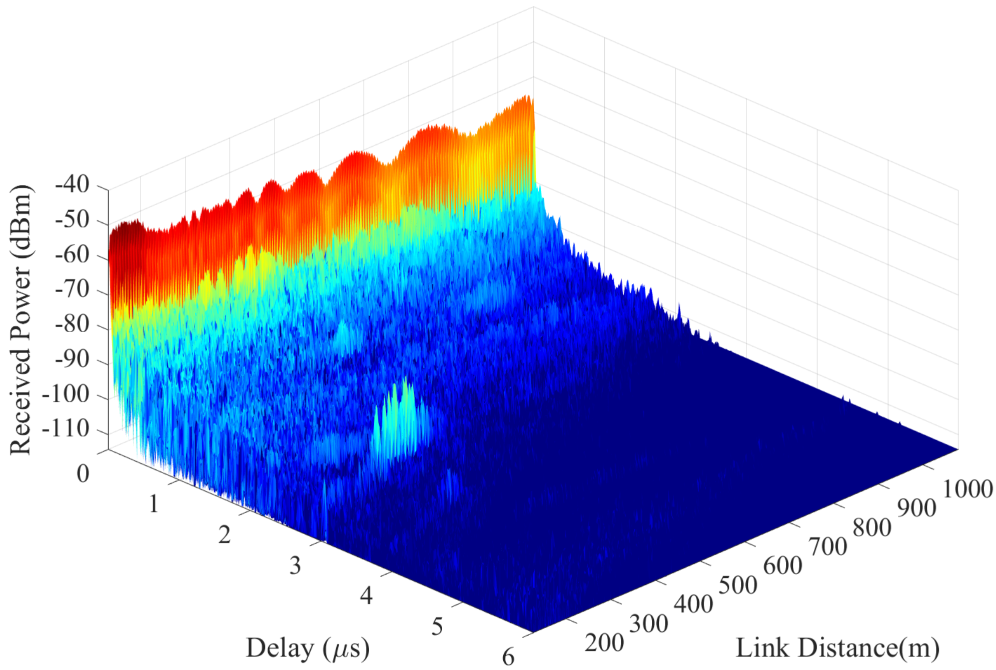

Figure 4.12 : 1750 A2G - Unprocessed PDP.

Fig. 4.13 shows the raw PDP results for 1750 MHz A2G. The results of the other A2G measurements are given in Figs. 4.15 and 4.17. At first glance, it is evident that the signal's strength varies as the distance changes. This fluctuation is analyzed in detail in the previous section. Secondly, it can be seen that the received reflections fade with increasing distance, but in some cases, dominant reflections occur and disappear. These reflections, which are always present and diminish with distance, come from close scatterers in the environment. Even if these reflections come from far distances, their effect on the channel is negligible because they are low-power. At this point, the strong reflections from far distances are the ones that are noteworthy.

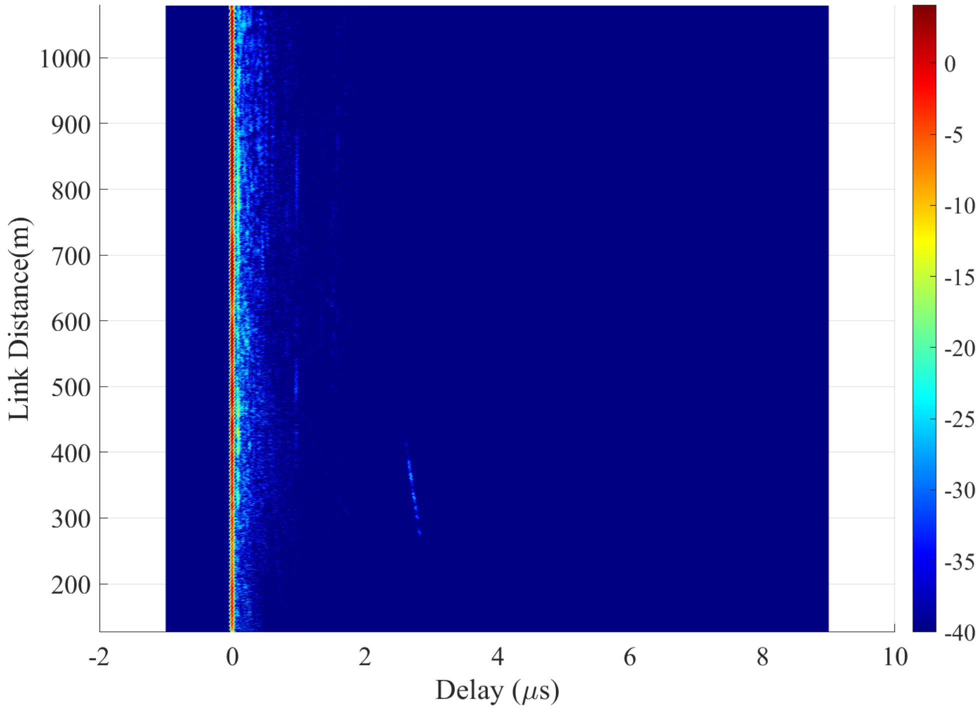

Figure 4.13 : 1750 A2G - PL normalized PDP.

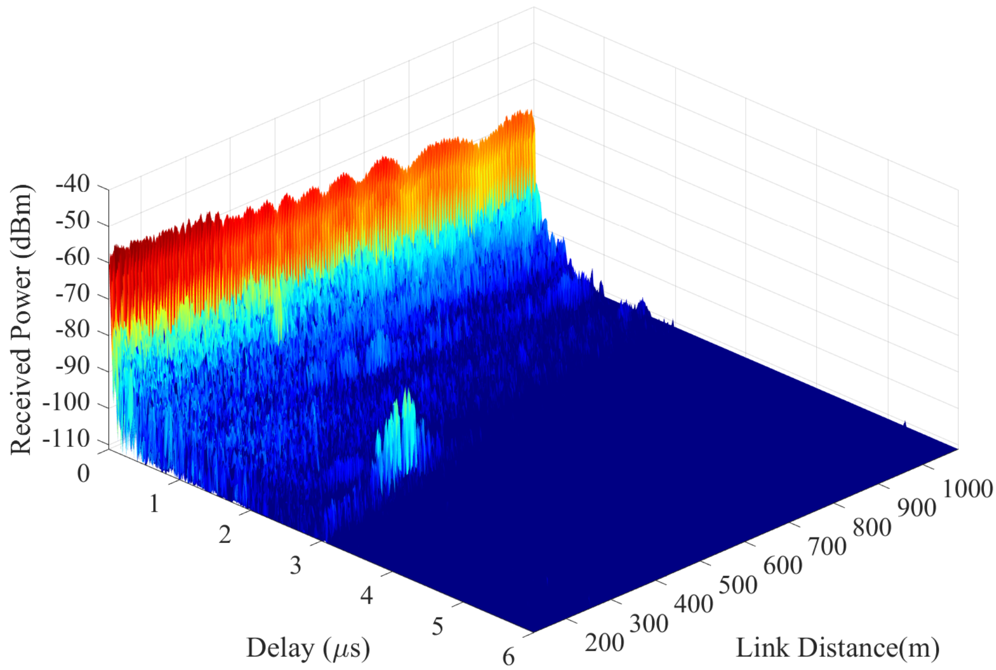

Figure 4.14 : 2560 A2G - Unprocessed PDP.

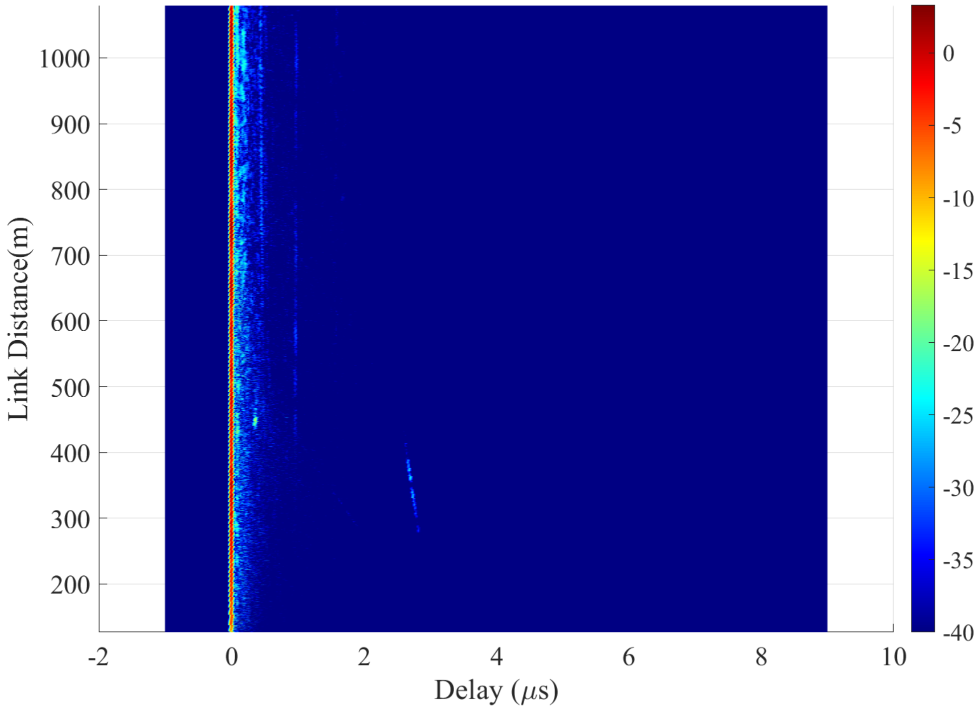

Figure 4.15 : 2560 A2G - PL normalized PDP.

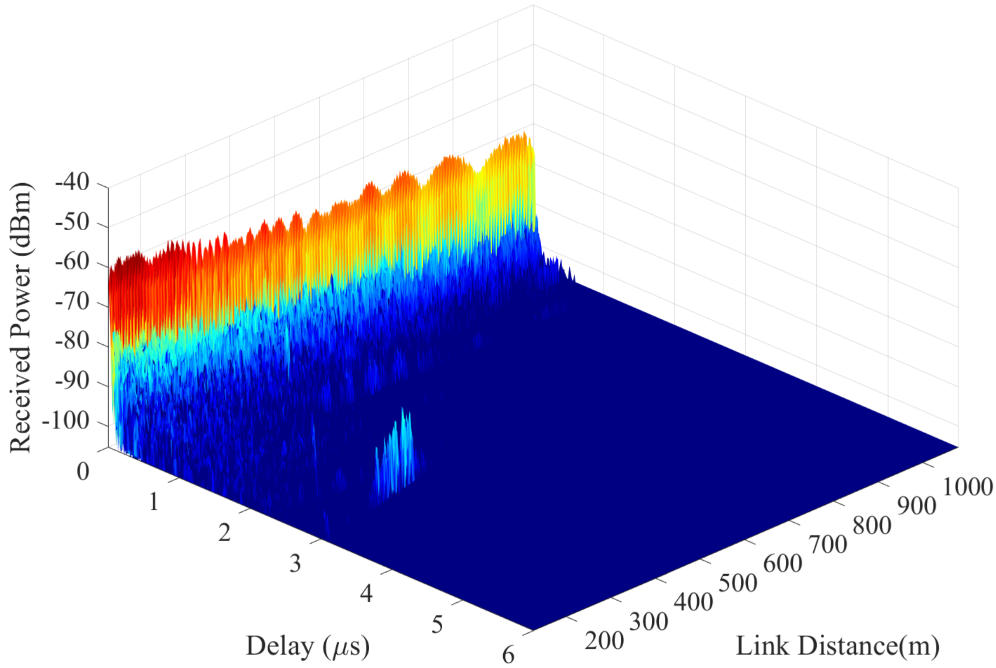

Figure 4.16 : 3500 A2G - Unprocessed PDP.

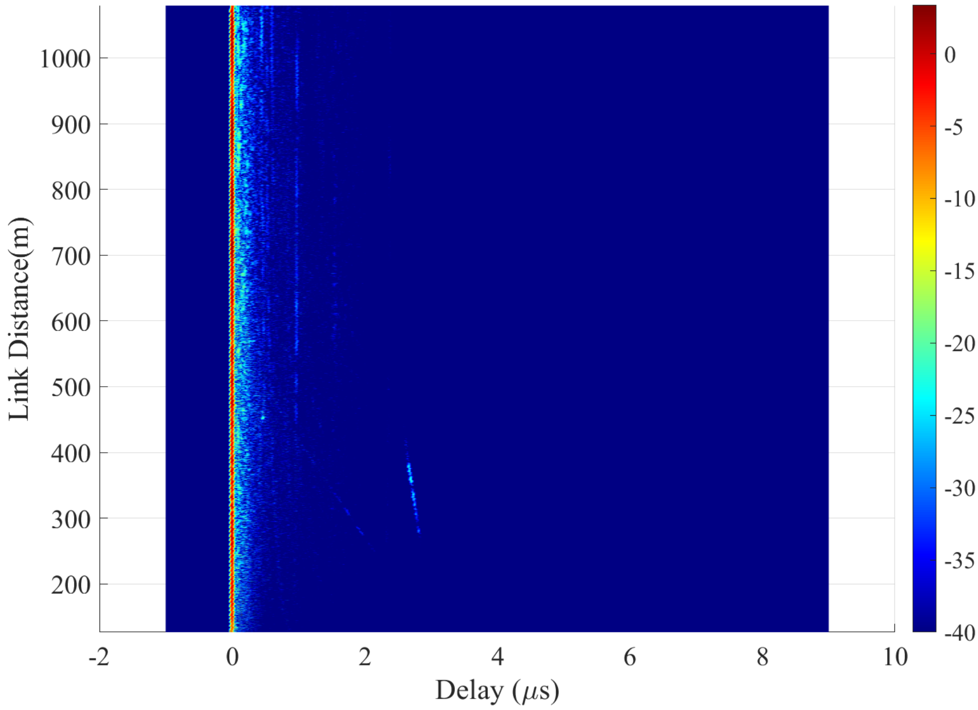

Figure 4.17 : 3500 A2G - PL normalized PDP.

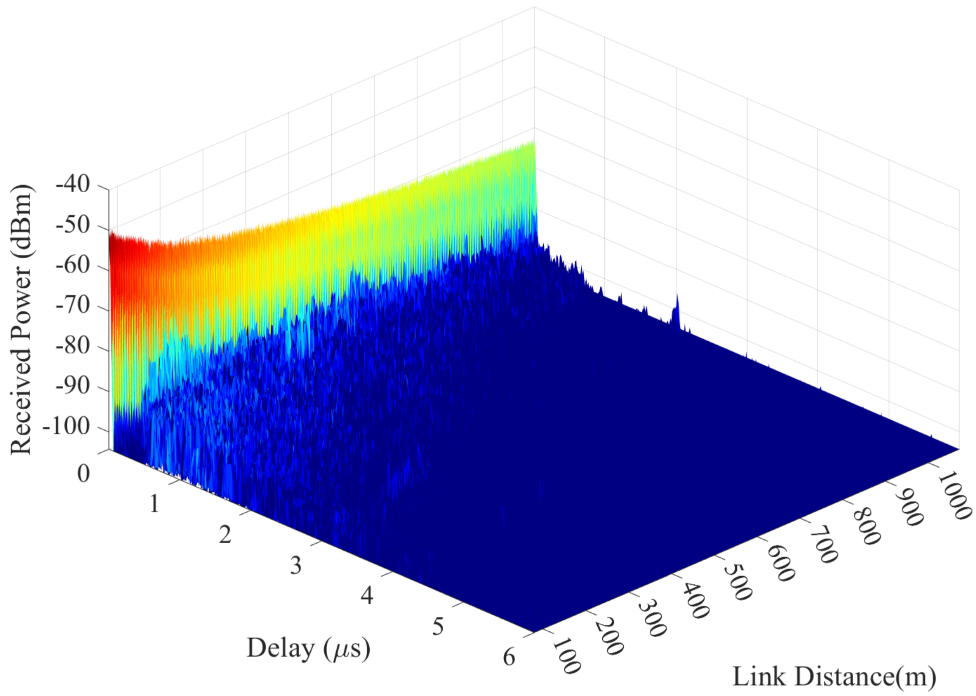

Figure 4.18 : 3500 A2A - Unprocessed PDP.

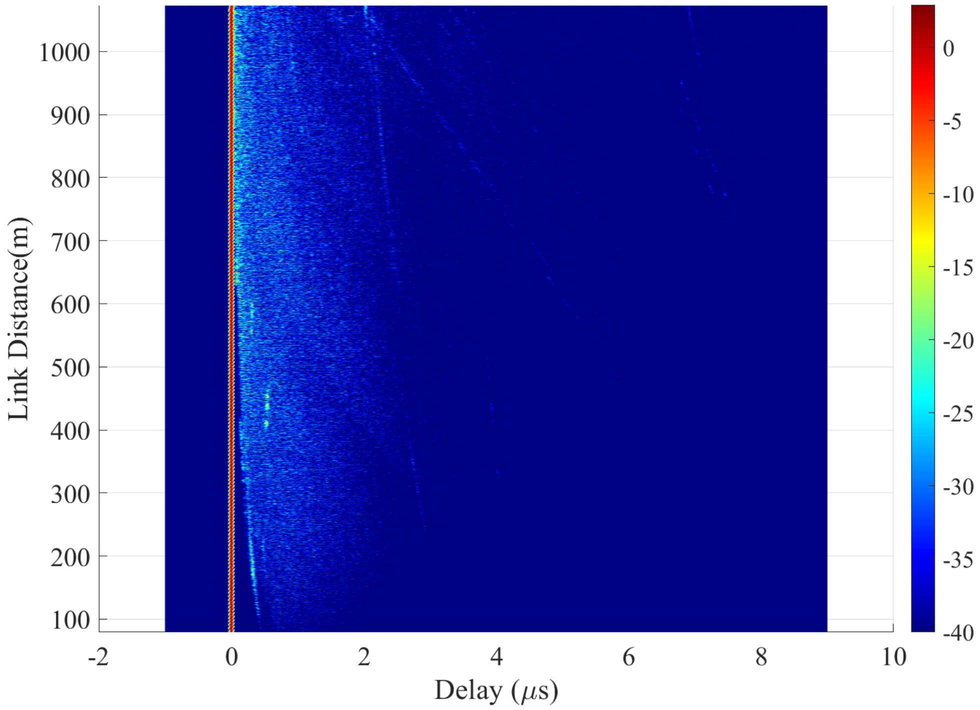

Figure 4.19 : 3500 A2A - PL normalized PDP.

In the A2G measurement results, a strong distant reflection occurred in the range of 300 to 400 meters. There are few surfaces in the measured environment that would cause such a strong reflection. Therefore, the time of arrival of this reflection is approximately 2771 ns when calculated geometrically at a direct distance of 353.6 meters. The CIR at the same distance is 2747.4 ns, as shown in Fig. 4.20. As a result, this strong reflection is considered to be the reflection from this building.

In the A2A PDP measurements shown in Figs. 4.18 and 4.19, several differences from the A2G cases are noteworthy.

First of all, the ground reflection separates from the direct path component. It can be seen in the Fig. 4.19. Upon taking a sample measurement at a distance of 174.8 meters, the geometrically calculated TDoA was determined to be 306 ns, while the measured TDoA was found to be 324 ns. These values indicate a similarity between the calculated and measured TDoA. As the distance between TX-D and RX-D increases, the ground reflection approaches the direct path as expected. Secondly, the reflections from the environment are coming from more distant than the A2G cases.

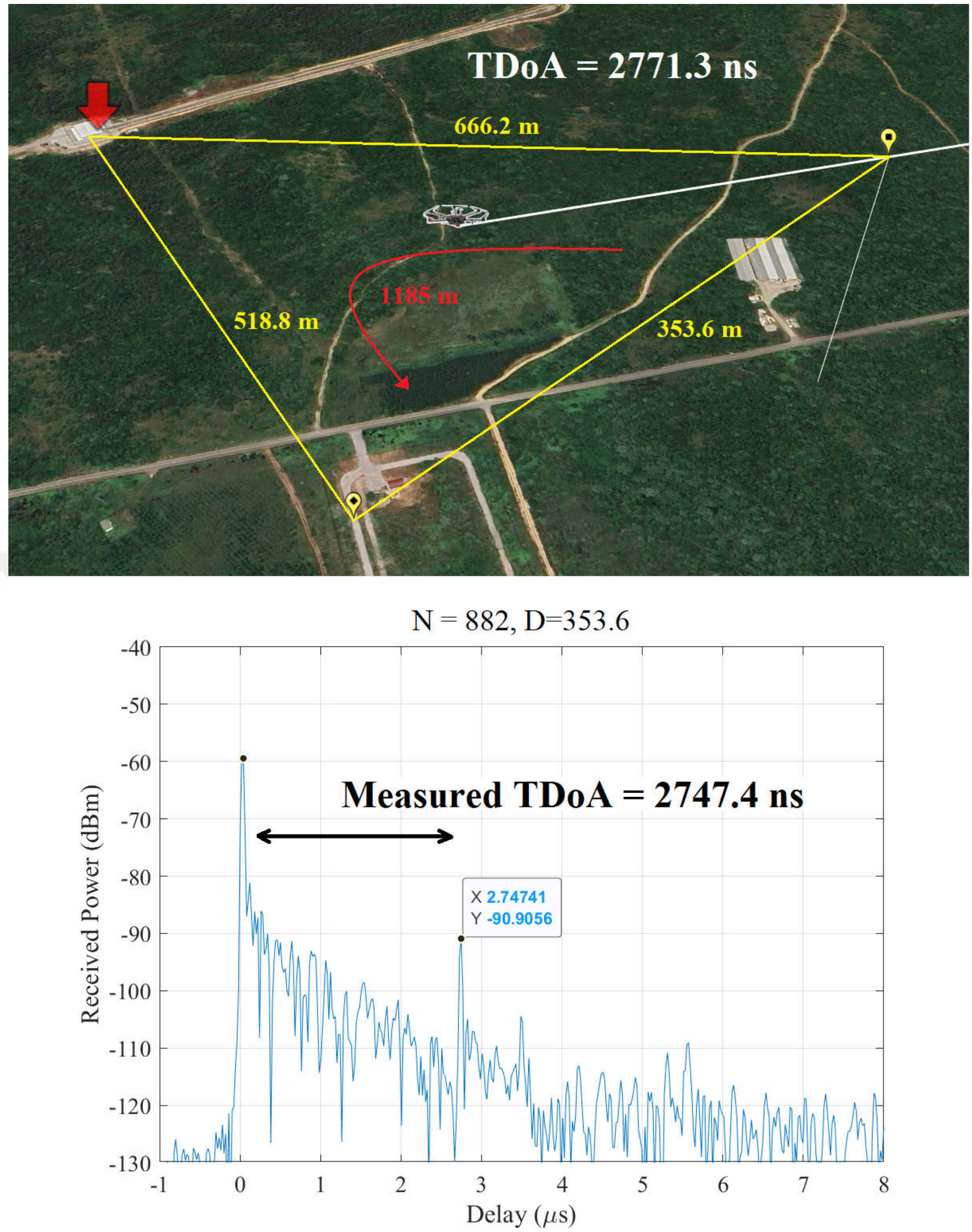

Figure 4.20 : Reflection point geometry and CIR at the point - A2G.

Secondly, reflections from the surroundings seem to come from further away than A2G cases and arrive at durations of up to 8 μs. This is mainly due to the fact that the receiver, like the transmitter, is at high altitude. Surfaces with high reflectivity (metal buildings, metal roofs, metal poles) are more numerous in the air than on the ground.

No matter how large these surfaces are, the measured signal strength is weak because the path loss is more dominant. In the current A2A measurement, reflections from the metal roofed building on the flight line were also seen on the PDP. The geometric analysis at the point where the reflection occurred and the CIR result obtained as a result of the measurement is shown in Fig. 4.21.

While the geometrically calculated TDoA is 516.7 ns, the TDoA value obtained from CIR is 563 ns. Considering that the reflection point used in the geometric analysis is approximate, the measurement results agree with the analytical value. In addition, the fact that the strong reflection on the PDP occurs 3 times in a row and the building has 3 roofs strongly suggests that these strong reflections come from the roof of the building.

In conclusion, our measurements on channels A2A and A2G indicate that buildings in rural areas can cause unexpected and sudden reflection points. In the next section, the impact of these sudden reflections on the RMS-DS and Ricean K-factors will be analyzed.

4.2.3 RMS delay spread & Ricean K-factor

Figures 4.22, 4.24, 4.26, and 4.28 show the RMS-DS results calculated on CIRs normalized by log-distance PL. These figures show the variation of the RMS-DS parameter over the course of the acquired measurement. Figures 4.23, 4.25, 4.27 and 4.29, on the other hand, show the values of the Ricean K-factor calculated over the CIR throughout the measurement. The results of the RMS-DS and Ricean K-factor analyses are summarized in Table 4.2.

As an example, Figure 4.22 shows the results of the RMS-DS analysis for the 1750 MHz A2G scenario. The effects of the strong and distant reflections mentioned in the previous section on the RMS-DS and Ricean K-factor are clearly visible. The strong reflection increases the RMS-DS value from its average value of about 30 ns to about 200 ns. After this reflection effect disappeared, the RMS-DS value fluctuated between 20-50 ns with the same trend as the FE2R-induced fluctuation on the main signal. The Ricean K-factor, on the other hand, averaged 18.9 dB in this measurement and was observed to drop down to 10 dB momentarily. Reflections causing sudden jumps

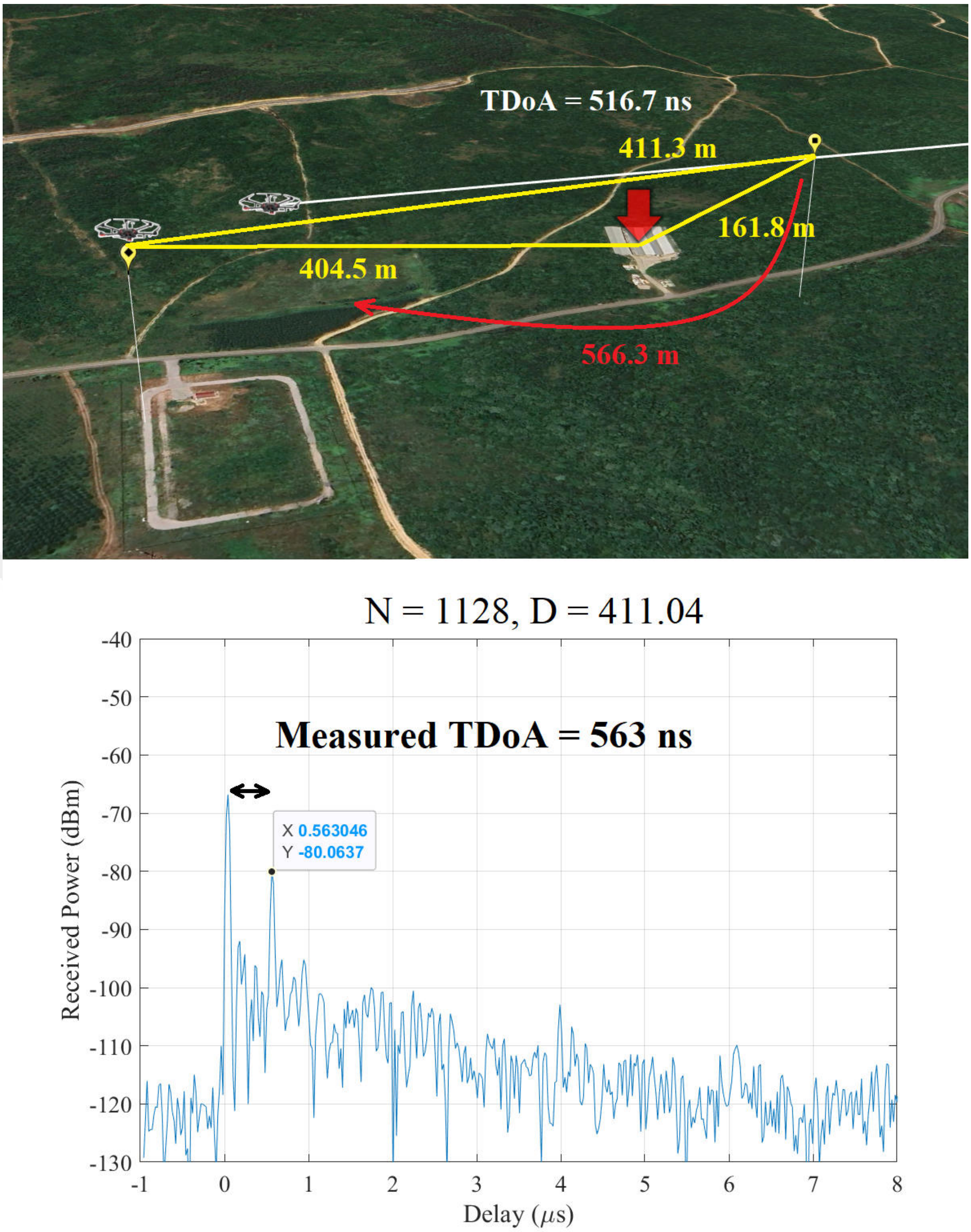

Figure 4.21 : Reflection point geometry and CIR at the point - A2A.

in the RMS-DS value had less impact on the Ricean K-factor due to its logarithmic nature.

The results of the analysis in the 2560 and 3500 MHz bands are shown in Figures 4.24, 4.25, 4.26 and 4.27. Similar effects to the measurements at 1750 MHz were observed.

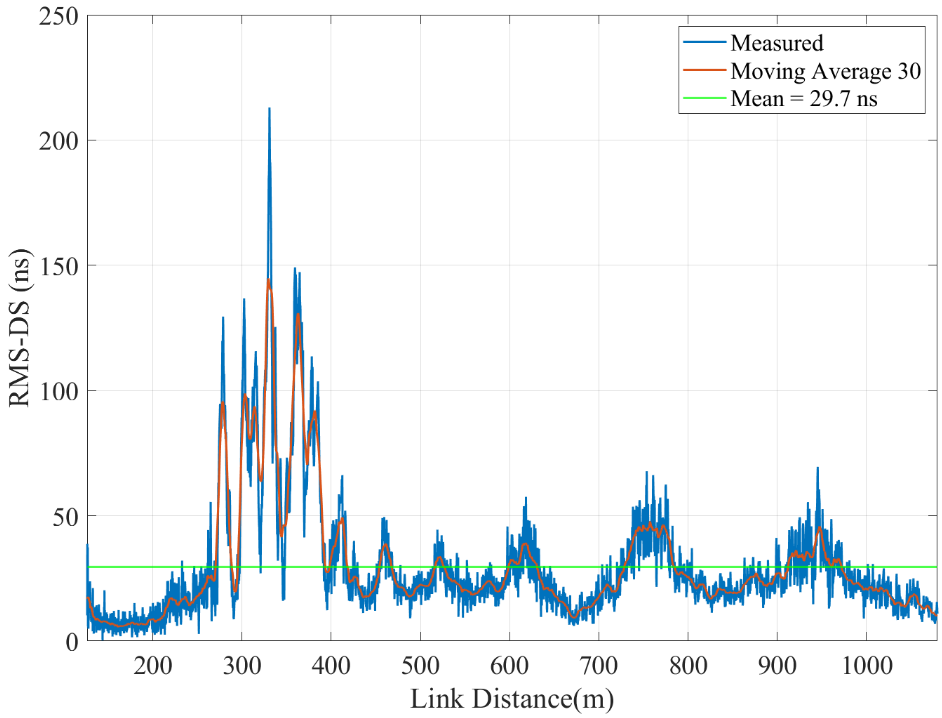

Figure 4.22 : 1750 A2G - RMS-DS vs. link distance.

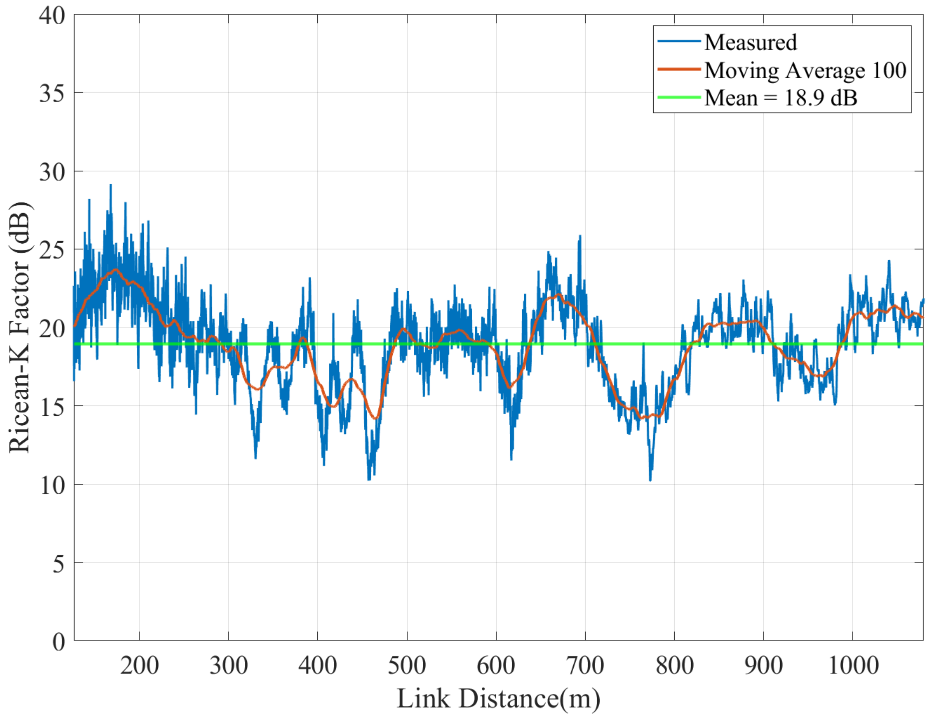

Figure 4.23 : 1750 A2G - Ricean K-factor vs. link distance.

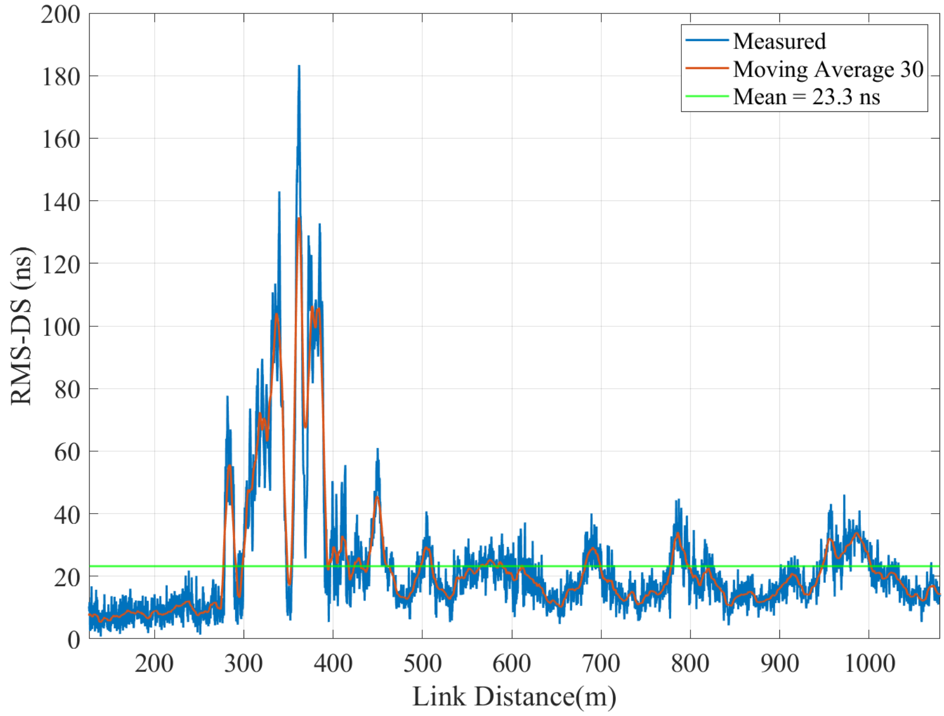

Figure 4.24 : 2560 A2G - RMS-DS vs. link distance.

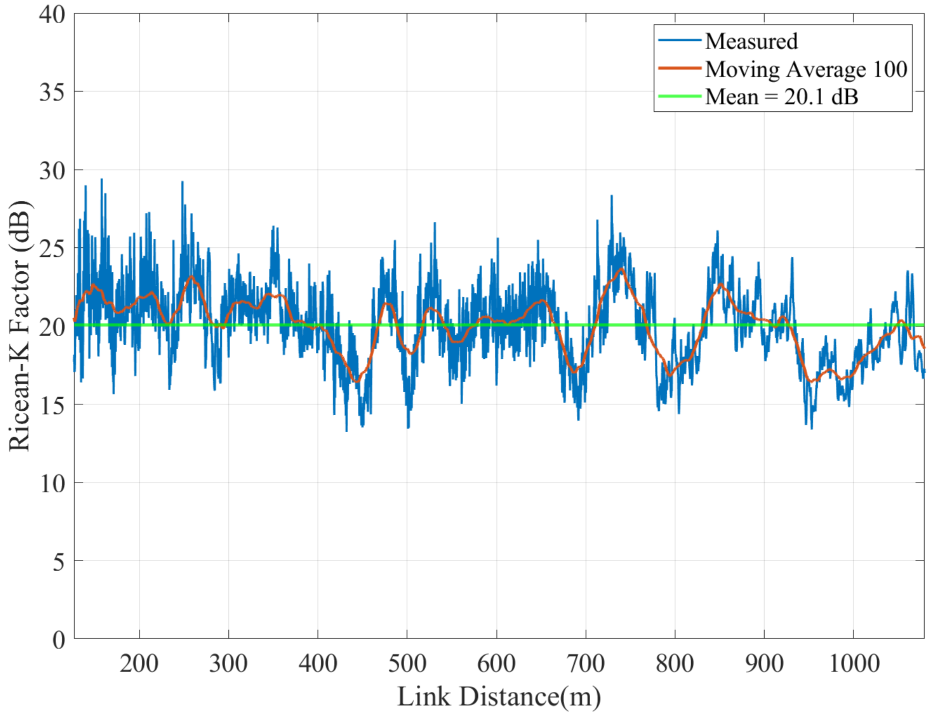

Figure 4.25 : 2560 A2G - Ricean K-factor vs. link distance.

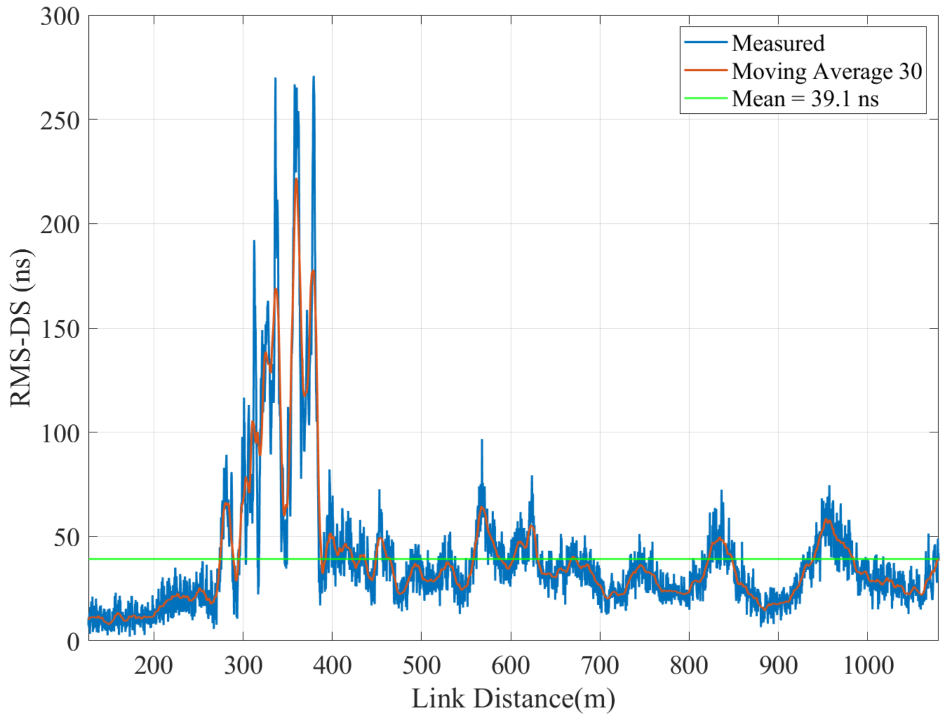

Figure 4.26 : 3500 A2G - RMS-DS vs. link distance.

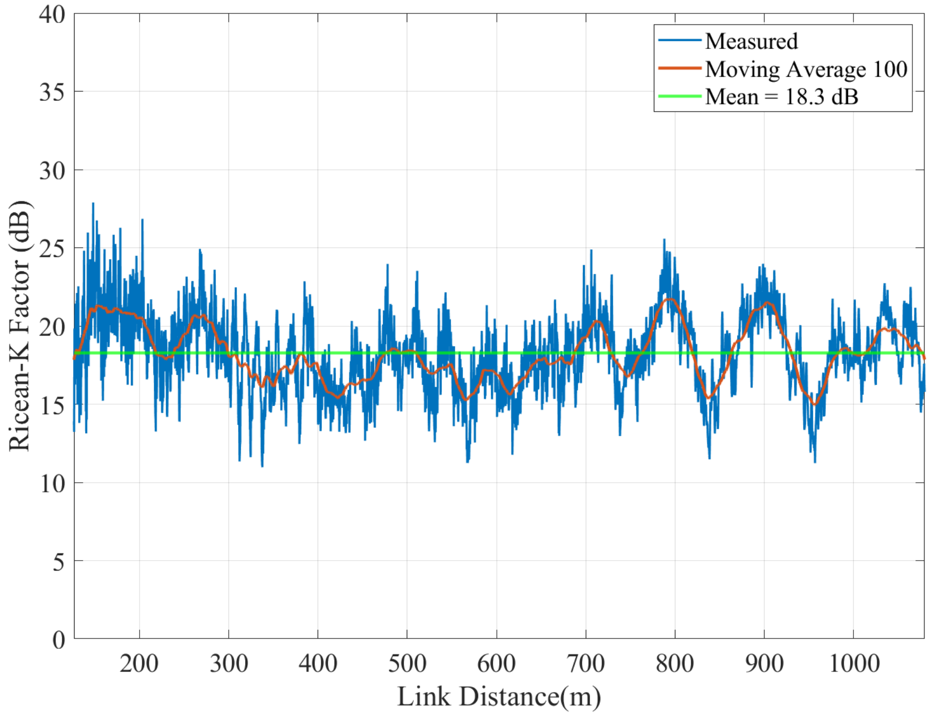

Figure 4.27 : 3500 A2G - Ricean K-factor vs. link distance.

The difference is that as the frequency increases, the surface resolution of the reflection increases and the RMS-DS value increases up to 180 ns for 2560 MHz and 250 ns for 3500 MHz in cases where full reflection occurs. In the case of ground reflection, the RMS-DS value fluctuates between 15-40 ns at 2560 MHz and between 20-65 ns at 3500 MHz. The Ricean K-factor was almost unaffected by strong reflections in these measurements, fluctuating between 15-25 dB at 2560 MHz and between 13-25 dB at 3500 MHz compared to the measurement in the 1750 MHz band.

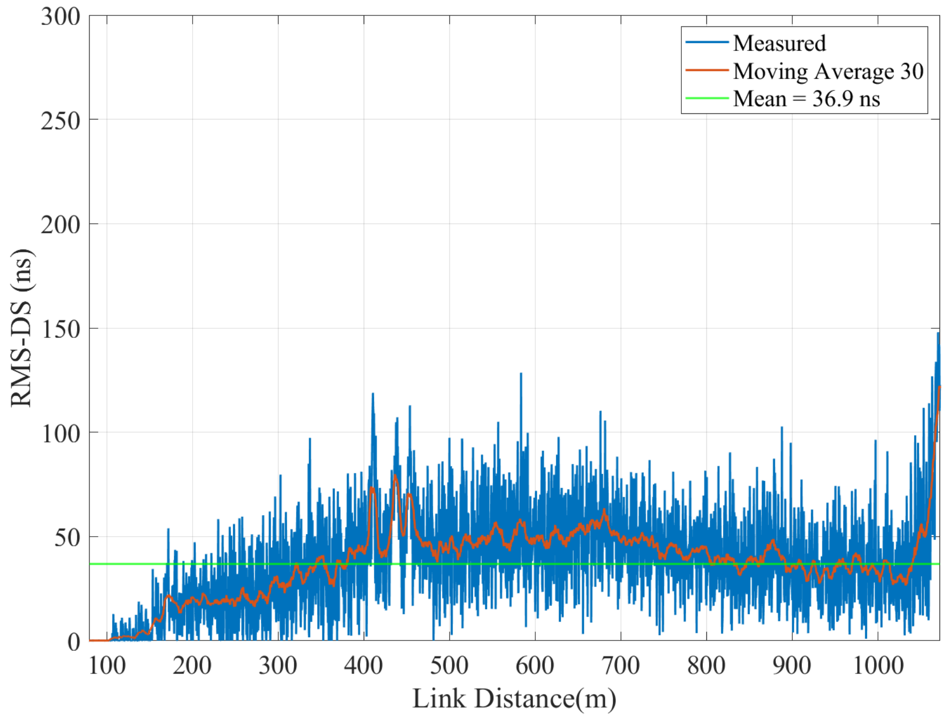

Figure 4.28 : 3500 A2A - RMS-DS vs. link distance.

The analysis results of the A2A measurement in the 3500 MHz band are shown in Figures 4.28 and 4.29. The first noticeable point in these results is that the RMS-DS value increases steadily in the first 400 meters. This is because the distance between the transmitter and receiver is small, so the signal coming directly from the path is much stronger than the distant reflections. Therefore, for the first 110 meters, the RMS-DS value is very close to zero, but as the distance increases, the average increases to around 40 ns. Another remarkable point is that the RMS-DS value fluctuates continuously between 20 and 120 ns throughout the measurement. This range is much larger compared to the previously analyzed A2G measurements. The high power reflections noted in the analysis of the PDP are also visible in the RMS-DS value. Since the

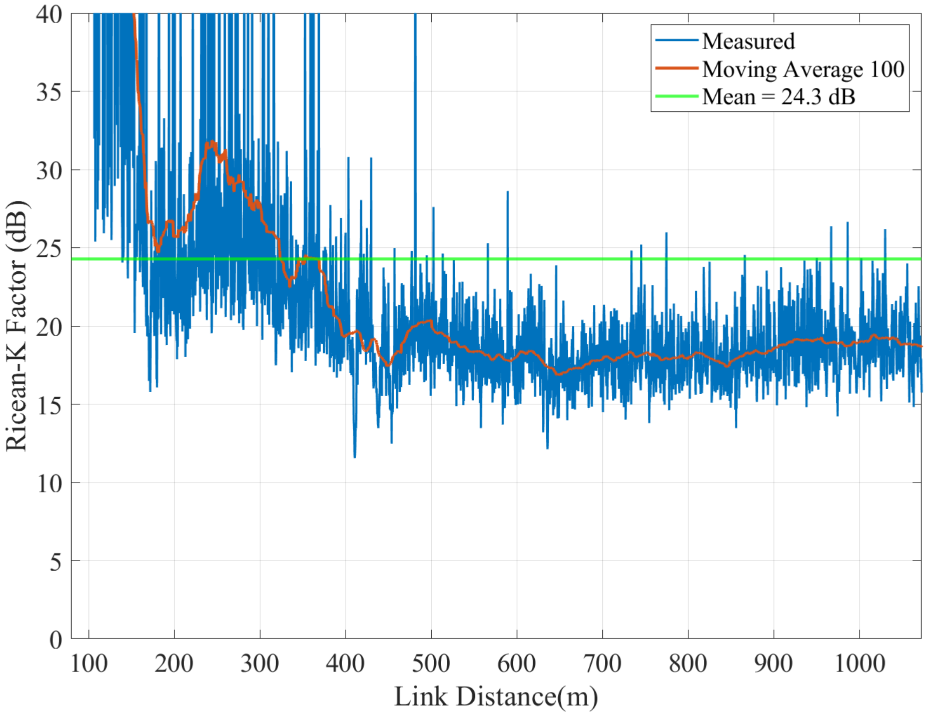

Figure 4.29 : 3500 A2A - Ricean K-factor vs. link distance.

instantaneous variations are high, these effects are more clearly visible with the moving average. Nevertheless, they do not have as high an impact as the peaks seen in the A2G measurements. Towards the end of the measurement, the RMS-DS value gradually increases from 40 ns to 150 ns as the power of a previously present low-power distant reflection point gradually increases.

On the other hand, it is noteworthy that at close distances, where the effect of the direct incoming signal is dominant, the Ricean K-factor is as high as 75 dB. Afterwards, it gradually decreased to 25 dB. As the influence of the direct signal fades, the Ricean K Factor decreases to 12 dB and remains around 18 dB for the rest of the measurement.

5. CONCLUSION AND FUTURE DIRECTIONS

In the information age, wireless communication is becoming increasingly vital. Research institutes and companies are racing to find more effective and efficient communication techniques. Among these technologies, vertical networks, where satellite, HAPS, and UAV platforms are included in communication networks, are among the current research topics. The main motivation is that the complexity of terrestrial communication channels is not the case in vertical networks. In addition, the coverage area increases as the altitude of the platform increases.

UAV platforms differ from other vertical network platforms at certain points. Their advantages are that they can be easily deployed and offer high bandwidth to the desired area. On the other hand, their disadvantages are their short flight time and low altitude. However, with current studies, these limitations are becoming less and less important. It stands out as an effective method to provide service to areas where there is no network or to illuminate blind spots in the coverage area.

In this study, wireless channel modeling and characterization for next-generation wireless communication system design and optimization are conducted. Firstly, the existing literature is reviewed, and the points where this study differs from other studies are emphasized. In addition, the models and equations to be used in channel modeling and analysis are given. In the second chapter, the channel sounder system developed for measurements is described. Next, the antenna, SDR, and mechanical subsystems of this system are discussed in detail. The third chapter focuses on the signal processing algorithms used, the practical problems encountered in their implementation, and the associated solutions. In addition, back-to-back calibration of the measurement system is explained. Results after the post-calibration and whether it is suitable for the measurements are shown. In the fourth chapter, measurement scenarios and analysis of the measurement results are presented. It is shown that the measurement area corresponds to rural areas, and the results indicate that this is the case. The measurement results were performed at 3 different frequencies and in 2 different configurations. In total, there are 4 scenarios which consist of three A2G and one A2A measurements. It is mentioned that the measured channels are on the same route. Accordingly, there is an opportunity to make a one-to-one comparison between the measurement results. Then, the narrowband characteristics of the channels and their agreement with the models were analyzed. It is observed that the measurements are within the theoretically expected levels. Then, the wideband characteristics of the channels are analyzed. It is observed that the channel effects are present at all frequencies and have different orders of impact. It is also observed that the A2A scenario differs from the A2G scenarios. The geometrical arrival points are calculated at the points where the reflection sources occur and vanish.

Possible future studies on this work are as follows:

- Taking measurements in regions with different terrain characteristics (cities, mountainous areas, sea surface, etc.) according to usage scenarios, such as applications that require high data rates, high reliability, low latency

- Performing measurements and analyses in frequency bands planned to be used in the future, outside of the cellular communication frequency bands currently used. In addition, measurements can also be targeted in frequency bands that can be used for different applications other than cellular communication.

- The designed channel measurement system operates in SISO structure. In future studies, analog and digital blocks that can work in multiple antenna structures can be aimed to be added to the system.

REFERENCES

[1] **Shakhatreh, H. and *et al.*** (2019). Unmanned Aerial Vehicles (UAVs): A survey on civil applications and key research challenges, *IEEE Access*, *7*, 48572–48634.

[2] **Zeng, Y.**, **Wu, Q. and Zhang, R.** (2019). Accessing from the sky: A tutorial on UAV communications for 5G and beyond, *Proceedings of the IEEE*, *107*(12), 2327–2375.

[3] **Mozaffari, M.**, **Saad, W.**, **Bennis, M.**, **Nam, Y.H. and Debbah, M.** (2019). A tutorial on UAVs for wireless networks: Applications, challenges, and open Problems, *IEEE Communications Surveys & Tutorials*, *21*(3), 2334–2360.

[4] **Matolak, D.W. and Fiebig, U.C.** (2019). UAV Channel Models: Review and Future Research, *2019 13th European Conference on Antennas and Propagation (EuCAP)*, pp.1–5.

[5] **Khawaja, W.**, **Guvenc, I.**, **Matolak, D.W.**, **Fiebig, U.C. and Schneckenburger, N.** (2019). A Survey of Air-to-Ground Propagation Channel Modeling for Unmanned Aerial Vehicles, *IEEE Communications Surveys & Tutorials*, *21*(3), 2361–2391.

[6] **Yan, C.**, **Fu, L.**, **Zhang, J. and Wang, J.** (2019). A Comprehensive Survey on UAV Communication Channel Modeling, *IEEE Access*, *7*, 107769–107792.

[7] **Schneckenburger, N.**, **Shutin, D.**, **Jost, T.**, **Walter, M.**, **Thiasiriphet, T.**, **Filip-Dhaubhadel, A. and Schnell, M.** (2014). From L-Band Measurements to a Preliminary Channel Model for APNT, volume 4.

[8] **Schneckenburger, N.**, **Jost, T.**, **Shutin, D. and Fiebig, U.C.** (2015). Line of sight power variation in the air to ground channel.

[9] **Matolak, D.W. and Sun, R.** (2017). Air–Ground Channel Characterization for Unmanned Aircraft Systems—Part I: Methods, Measurements, and Models for Over-Water Settings, *IEEE Transactions on Vehicular Technology*, *66*(1), 26–44.

[10] **Sun, R. and Matolak, D.W.** (2017). Air–Ground Channel Characterization for Unmanned Aircraft Systems Part II: Hilly and Mountainous Settings, *IEEE Transactions on Vehicular Technology*, *66*(3), 1913–1925.

[11] **Matolak, D.W. and Sun, R.** (2017). Air–Ground Channel Characterization for Unmanned Aircraft Systems—Part III: The Suburban and Near-Urban Environments, *IEEE Transactions on Vehicular Technology*, *66*(8), 6607–6618.

[12] **Sun, R.**, **Matolak, D.W. and Rayess, W.** (2017). Air-Ground Channel Characterization for Unmanned Aircraft Systems—Part IV: Airframe Shadowing, *IEEE Transactions on Vehicular Technology*, *66*(9), 7643–7652.

[13] **Stofik, N.**, **Matolak, D.W. and Sahin, A.** (2022). Measurement and Modeling of Low-Altitude Air-Ground Channels in Two Frequency Bands, *2022 Integrated Communication, Navigation and Surveillance Conference (ICNS)*, pp.1–10.

[14] **Amorim, R.**, **Nguyen, H.**, **Mogensen, P.**, **Kovács, I.Z.**, **Wigard, J. and Sørensen, T.B.** (2017). Radio Channel Modeling for UAV Communication Over Cellular Networks, *IEEE Wireless Communications Letters*, *6*(4), 514–517.

[15] **Yanmaz, E.**, **Kuschnig, R. and Bettstetter, C.** (2011). Channel measurements over 802.11a-based UAV-to-ground links, *2011 IEEE GLOBECOM Workshops (GC Wkshps)*, pp.1280–1284.

[16] **Hayat, S.**, **Yanmaz, E. and Bettstetter, C.** (2015). Experimental analysis of multipoint-to-point UAV communications with IEEE 802.11n and 802.11ac, *2015 IEEE 26th Annual International Symposium on Personal, Indoor, and Mobile Radio Communications (PIMRC)*, pp.1991–1996.

[17] **Willink, T.J.**, **Squires, C.C.**, **Colman, G.W.K. and Muccio, M.T.** (2016). Measurement and Characterization of Low-Altitude Air-to-Ground MIMO Channels, *IEEE Transactions on Vehicular Technology*, *65*(4), 2637–2648.

[18] **Badi, M.**, **Rajan, D. and Camp, J.** (2021). Measurement-based Characterization of Human Body Impact on Ultra-low UAV-to-Ground Channels, *MILCOM 2021 - 2021 IEEE Military Communications Conference (MILCOM)*, pp.556–561.

[19] **Moraitis, N.**, **Psychogios, K. and Panagopoulos, A.D.** (2023). A Survey of Path Loss Prediction and Channel Models for Unmanned Aerial Systems for System-Level Simulations, *Sensors*, *23*(10), `https://www.mdpi.com/1424-8220/23/10/4775`.

[20] **Walter, M.**, **Gligorević, S.**, **Detert, T. and Schnell, M.** (2010). UHF/VHF air-to-air propagation measurements, *Proceedings of the Fourth European Conference on Antennas and Propagation*, pp.1–5.

[21] **GmbH, S.M.T.** (2015). *Saab Medav Technologies RUSK MIMO Channel Sounder*, `https://web.archive.org/web/20151222104414/http://www.medav.de/fileadmin/redaktion/documents/English/SMT_rusk_mimo.pdf`, accessed: December 21, 2023.

[22] **Walter, M. and Schnell, M.** (2011). Statistical distribution of line-of-sight and reflected path in the aeronautical channel, *2011 IEEE/AIAA 30th Digital Avionics Systems Conference*, pp.4D1–1–4D1–9.

[23] **Bellido-Manganell, M.A., Fiebig, U.C. and Walter, M.** (2022). Aircraft-to-Aircraft Channel Measurements in the VHF/UHF Band: Analysis of the Line-of-Sight and Lake-Reflected Channel Components, *2022 IEEE 96th Vehicular Technology Conference (VTC2022-Fall)*, pp.1–7.

[24] **Takizawa, K., Ono, F., Suzuki, M., Tsuji, H. and Miura, R.** (2014). Measurement on S-band radio propagation characteristics for unmanned aircraft systems, *The 8th European Conference on Antennas and Propagation (EuCAP 2014)*, pp.3068–3072.

[25] **Liu, T., Zhang, Z., Jiang, H., Qian, Y., Liu, K., Dang, J. and Wu, L.** (2019). Measurement-Based Characterization and Modeling for Low-Altitude UAV Air-to-Air Channels, *IEEE Access*, *7*, 98832–98840.

[26] **Ede, B., Kaplan, B., Kahraman, , Keşir, S., Yarkan, S., Ekti, A.R., Baykaş, T., Görçin, A. and Çırpan, H.A.** (2022). Measurement-Based Large Scale Statistical Modeling of Air–to–Air Wireless UAV Channels via Novel Time–Frequency Analysis, *IEEE Wireless Communications Letters*, *11*(1), 136–140.

[27] **Becker, D. and Fiebig, U.C.** (2022). Measurement Based Identification of MPCs in an Urban Drone-to-Drone Propagation Scenario, *2022 16th European Conference on Antennas and Propagation (EuCAP)*, pp.1–5.

[28] **Becker, D., Fiebig, U.C. and Schalk, L.** (2020). Wideband Channel Measurements and First Findings for Low Altitude Drone-to-Drone Links in an Urban Scenario, *2020 14th European Conference on Antennas and Propagation (EuCAP)*, pp.1–5.

[29] **Guan, Z. and Kulkarni, T.** (2019). On the Effects of Mobility Uncertainties on Wireless Communications between Flying Drones in the mmWave/THz Bands, *IEEE INFOCOM 2019 - IEEE Conference on Computer Communications Workshops (INFOCOM WKSHPS)*, pp.768–773.

[30] **Boegl, T., Rautenberg, M., Haindl, B., Rihacek, C., Meser, J., Fantappie, P., Pringvanich, N., Micallef, J., Hauf, K., MacBride, J., Sacre, P., van den Einden, B., Gräupl, T. and Schnell, M.** (2019). LDACS White Paper - A Roll-out Scenario, **Working Paper DCIWG/3-IP01**, International Civil Aviation Organization, prepared by PT-T Participants.

[31] **Rappaport, T.S.** (2002). *Wireless communications: Principles and practice*, Prentice Hall communications engineering and emerging technologies series.

[32] **Parsons, J.D.** (2001). *The Mobile Radio Propagation Channel*, `http://dx.doi.org/10.1002/0470841524`.

[33] **Pirkl, R.J. and Durgin, G.D.** (2008). Optimal sliding correlator channel sounder design, *IEEE Trans. Wireless Commun.*, *7*(9), 3488–3497.

[34] **Collins, T.F.**, **Getz, R.**, **Pu, D. and Wyglinski, A.M.** (2018). *Software-Defined Radio for Engineers*, Artech House.

[35] **Devices, A.** (2023). RF Agile Transceiver Data Sheet AD9363, **Technical Report**, Analog Devices, `https://www.analog.com/media/en/technical-documentation/data-sheets/AD9363.pdf`.

[36] **ITU-R, Recommendations.** (2019). *Multipath propagation and parameterization of its characteristics*, Recommendation P.1407-8, `tinyurl.com/3ny6c8ur`.

[37] **Ju, S.**, **Xing, Y.**, **Kanhere, O. and Rappaport, T.S.** (2022). Sub-Terahertz Channel Measurements and Characterization in a Factory Building, *IEEE International Conference on Communications*, pp.2882–2887.

CURRICULUM VITAE

Name Surname: Ubeydullah ERDEMİR

EDUCATION:

- **B.Sc.:** 2020, Istanbul Technical University, Faculty of Electrical and Electronics, Department of Electronics and Communication Engineering

PROFESSIONAL EXPERIENCE AND REWARDS:

- Sep 2018 - Team Leader of the VIST, First Place & Won 6000$ Prize in Swarm UAV Category - TeknoFest 2018 Competition
- Oct 2020 - Present Researcher at The Scientific and Technological Research Council of Turkey (Informatics and Information Security Research Center)

PUBLICATIONS, PRESENTATIONS AND PATENTS ON THE THESIS:

- **Erdemir U., Kaplan B., Hokelek İ., Görçin A. and Çırpan, H. A.,** 2023. Measurement-based Channel Characterization for A2A and A2G Wireless Drone Communication Systems. *International Congress - IEEE 97th Vehicular Technology Conference (VTC2023-Spring)*, Florence, Italy, 2023, pp. 1-6, doi: 10.1109/VTC2023-Spring57618.2023.10199853.

OTHER PUBLICATIONS, PRESENTATIONS AND PATENTS:

- **Erkek, N. K., Balcı E., Halay B., Erdemir U., Görçin A. and Çırpan, H. A.,** 2022. Measurement-Based Cellular Band Air–to–Ground Channel Modeling for UAVs. *IEEE 96th Vehicular Technology Conference (VTC2022-Fall)*, London, United Kingdom, 2022, pp. 1-6, doi: 10.1109/VTC2022-Fall57202.2022.10012846.
- **Çelebi, B. A., Erdemir U. and Görçin A.,** 2022. Comparison of Relay and Reconfigurable Intelligent Surfaces for Millimeter-Wave Communication Systems. *30th Signal Processing and Communications Applications Conference (SIU)*, Safranbolu, Turkey, 2022, pp. 1-4, doi: 10.1109/SIU55565.2022.9864821.